Texture and chemistry of pyrite at Chah Zard epithermal gold–silver deposit, Iran

Hossein Kouhestani [a,1], Majid Ghaderi [a,*], Ross R. Large [b], Khin Zaw [b]

[a] Department of Economic Geology, Tarbiat Modares University, Tehran 14115-175, Iran
[b] CODES ARC Centre of Excellence in Ore Deposits, University of Tasmania, Hobart 7001, Australia

A B S T R A C T

Gold mineralization at Chah Zard, Iran, is mostly concentrated in breccia and veins, and is closely associated with pyrite. Optical and scanning electron microscopy-backscattered electron observations indicate four different pyrite types, each characterized by different textures: porous and fractured py1, simple-zoned, oscillatory-rimmed, framboidal and fibrous py2, colloform py3, and inclusion-rich py4. Laser ablation ICP–MS analysis and elemental mapping reveal the presence of invisible gold in all pyrite types. The highest concentrations (161–166 ppm Au) are found in py2 and py4, which correlate with the highest As concentrations (73,000–76,000 ppm). In As-poor grains, Au concentrations decrease by about two orders of magnitude. Copper, Pb, Zn, Te, Sb, and Ag occur with invisible gold, suggesting that at least part of the gold occurs in nanoparticles of sulfosalts of these metals and metalloids. Gold distribution patterns suggest that only negligible Au was originally trapped in py1 from the initial ore fluids. However, most, if not all, Au was transported and deposited during subsequent overprinting hydrothermal fluid flow in overgrowth rims around the margins of the py2 and within microfractures of py4 grains. Oscillatory zonation patterns for Co, Ni, Sb, Cu, Pb, and Ag in pyrite reflect fluctuations in the hydrothermal fluid chemistry. The LA-ICP–MS data reveal that Cu, Pb and Ag show systematic variations between different pyrite types. Thus, Cu/Pb and Pb/Ag ratios in pyrite may provide a potentially powerful exploration vector to epithermal gold mineralization at Chah Zard district and elsewhere.

© 2017 Elsevier B.V. All rights reserved.

1. Introduction

Chah Zard is a low- to intermediate-sulfidation epithermal gold–silver deposit, formed within a late Miocene, calc-alkaline to high-K calc-alkaline volcanic complex in central Iran (Kouhestani, 2011; Kouhestani et al., 2012). The Chah Zard deposit is the first reported occurrence of a pipe-like, breccia-hosted epithermal gold–silver deposit in Iran with a proven reserve of ~2.5 Mt @ 1.7 g/t Au and 12.7 g/t Ag and an estimated reserve of 6.3 Mt @ 0.77 g/t Au and 10.8 g/t Ag (Kouhestani, 2011; Kouhestani et al., 2012). Before 2004, the area was not known for gold mineralization and more recent mining activities had focused on small silver-bearing quartz-hosted sphalerite–galena–(pyrite) veins located outside the main gold-mineralized breccia zones. Ore formation at Chah Zard is spatially and genetically associated with late Miocene rhyolitic subvolcanic/porphyry (Kouhestani

et al., 2012), and hydrothermal fluids related to the Au-Ag deposition are characterized by a mixture of magmatic fluids with meteoric water under epithermal conditions (Ghaderi et al., 2012a,b; Kouhestani et al., 2015). Pyrite is the most abundant sulfide in the Chah Zard deposit and is widespread in all paragenetic stages. It is the most important Au-hosting mineral in ore zones as gold occurs principally as inclusions within, and intergrown with, pyrite. Pyrite in Chah Zard is also a host of 'invisible' gold (structure-hosted or nanoparticulate gold; Kouhestani, 2011).

As one of the most common constituents of ore-bearing mineral assemblages, pyrite has the potential to provide useful information on ore-forming processes (Koglin et al., 2010). A significant body of data is now available on trace element distributions in pyrite by proton microprobe (Przybyłowicz et al., 1995; Reimold et al., 2004; Agangi et al., 2013) and laser-ablation inductively coupled plasma mass spectrometry (LA-ICP–MS, Koglin et al., 2010; Zhao et al., 2011; Bi et al., 2011; Large et al., 2007, 2009, 2013; Cook et al., 2009, 2013; Agangi et al., 2013; Velásquez et al., 2014), indicating that pyrite can contain a multitude of other elements in trace amounts. Therefore, if the pyrite precipitated directly from the ore-forming fluid, the trace element composition of the pyrite

can provide useful information about the ore-forming fluids and processes (Zhao et al., 2011). We provide the first textural and LA-ICP–MS data on Au and other trace element concentrations in pyrite from the Chah Zard deposit. In this contribution, we show that systematic differences exist between different pyrite types with regard to the abundances of several trace elements and we investigate these textural and compositional variations to better understand the residence of gold in the sulfide paragenesis in the Chah Zard epithermal gold-silver deposit and to characterize the ore-forming processes. This study shows that the chemical variations of pyrite give information on the evolution stages of epithermal ore systems, and addressing these variations along with their correlation with pyrite textures, provides a possibility to use it as a potential exploration vector to epithermal gold ore.

2. Geotectonic setting

The Chah Zard gold-silver deposit is located in the central part of the Urumieh-Dokhtar Magmatic Arc (UDMA), a >2000 km-long and 100 km-wide belt which forms an Andean-type volcano-plutonic arc (Berberian et al., 1982; Sengör, 1990; Alavi, 1994) associated with subduction of Neo-Tethyan oceanic crust along the strike of the Zagros Mountains (Richards et al., 2006; Shahabpour, 2007; Omrani et al., 2008). Magmatic activity started from Eocene time and continued to the present (e.g., Berberian and Berberian, 1981; Berberian and King, 1981; Bina et al., 1986; Omrani et al., 2008; Dargahi et al., 2010), with a peak during the Oligocene to Miocene (Agard et al., 2005, 2011).

The Chah Zard deposit is hosted by an intermediate to felsic volcanic complex of late Miocene age (Kouhestani et al., 2012) (Fig. 1). The volcanic rocks consist mainly of large-scale (>6 km across) dark gray andesite–trachyandesite flow dome system that is intruded by several co-axial dacitic to rhyolitic porphyries in the central parts of the system. Emplacement of the rocks from this high-K calc-alkaline complex took place at 6.2 ± 0.2 Ma (LA-ICP–MS U–Pb zircon ages, Kouhestani et al., 2012). Kouhestani (2011) and Kouhestani et al. (2012) have shown that the volcanic rocks were strongly affected by hydrothermal alteration in the core of the system. The volcanic complex is bound to the northwest, west, and southeast by Eocene and Oligo–Miocene rocks and to the north by Miocene aged rocks (Fig. 1). The Eocene rocks consist mainly of folded tuff beds that are intercalated with marl, sandstone and shale. Oligo–Miocene rocks are exposed only in the southeastern side of the Chah Zard area. They comprise mainly marl, tuffaceous sandstone and various conglomerates. These units were thrust over Miocene clastic rocks along the NW–SE-trending Chah Zard fault (Fig. 1). Miocene rocks are widespread in the northern, eastern, and southeastern parts of the area. They are composed of folded unconsolidated conglomerate, sandstone, and marl and are equivalent to the Upper Red Formation in Central Iran (Kouhestani, 2011).

The main geologic structures of the Chah Zard area are a series of tensile-shear NW–SE and NE–SW-trending strike-slip fault systems (Fig. 1). These faults are part of the shear zones, transtensional pull-apart basins, and other syntectonic structures southwest of Yazd, associated to the main Dehshir-Baft fault (DBF) system (insert of Fig. 1). The NW–SE-trending faults are the most prominent in terms of length; and are first-order structures related to the DBF. This group is synthetic to, and has similar dextral displacements as, the DBF, but their strike makes an average angle of 35° to the trend of the DBF. The NE–SW-trending faults are small second-order superimposed structures with small, inferred sinistral displacements and are antithetic to the DBF. The intersection of these two structures was the locus for magma emplacement and ore formation in the area during the late

Miocene, as has been suggested for orogenic belts elsewhere (e.g., Richards et al., 2001; Tosdal and Richards, 2001).

3. Characteristics of the Chah Zard deposit

Chah Zard is a breccia-hosted low- to intermediate-sulfidation epithermal gold-silver deposit (Kouhestani et al., 2012, 2015). Brecciation and mineralization at Chah Zard occurred synchronous with, and subsequent to, shallow emplacement of rhyolite porphyries. Previous studies (Kouhestani, 2011; Kouhestani et al., 2012) revealed three types of breccia at Chah Zard: volcaniclastic, polymictic, and mixed monomictic to polymictic breccia. The polymictic breccias generated bulk-mineable ore, and the highest grade and most extensive mineralization occurs in two polymictic, pipe-like breccia bodies with elliptical horizontal sections of 500 × 250 m and 300 × 200 m. The volcaniclastic breccia is largely barren.

Mineralization at Chah Zard has been described by Kouhestani (2011) and Kouhestani et al. (2012, 2015). The gold–silver ores are hosted mainly by breccia cements, sheeted and conjugate veins, and disseminated sulfides and sulfosalts. A U–Pb zircon age of 6.2 ± 0.2 Ma for emplacement of the rhyolitic magmas is interpreted as the maximum age of Au–Ag mineralization at Chah Zard (Kouhestani et al., 2012). Ore minerals are dominated by pyrite and arsenian pyrite, with lesser amounts of chalcopyrite, galena, sphalerite, and locally arsenopyrite. Other ore minerals include marcasite, native gold, electrum, and silver sulfosalts. Chalcocite, covellite, digenite, and different iron and manganese oxides have been identified in the oxidized zone. Most ore minerals form predominately anhedral grains, although some display euhedral or subhedral textures. They occur as disseminations, veinlets, and massive accumulations in veins and hydrothermally cemented breccias, or as matrix to silicified breccia clasts, with replacement, colloform, zoned, framboidal, fibrous and brecciated textures. Gangue minerals include quartz, adularia, sericite (both fine-grained hydromuscovite and illite), smectite, chlorite and minor carbonate (calcite, ankerite, siderite and minor dolomite), and generally occur as fine-grained assemblages; some are, however, medium- and coarse-grained. They occur as massive, banded, brecciated, vuggy structures, or as veinlets and stockwork veins, with comb, cockade, crustiform, colloform and in places with plumose textures.

Hydrothermal alteration is zoned around breccias and veins (Kouhestani et al., 2012). The alteration assemblages grade from proximal quartz-adularia-pyrite through illite-quartz-pyrite, and illite/smectite-pyrite-carbonate to distal chlorite-calcite ± illite ± quartz. The quartz-adularia and illite alteration types are spatially and temporally closely associated with high-grade gold mineralization, whereas carbonate alteration is found associated with low-grade ore zones. There is a late overprint of supergene alteration (advanced argillic: hematite, limonite, jarosite, gypsum, kaolinite and rare alunite) blanketing the vein and breccia system. Alteration patterns at Chah Zard were controlled by lithologic units, structure, and host-rock permeability (Kouhestani, 2011).

Five stages of mineral precipitation are recognized at Chah Zard (Kouhestani et al., 2012, Table 1). Stage 1 is represented by pyrite-quartz-illite ± chalcopyrite–cemented veins (<5 mm in width) and breccias. This stage is related to hydrothermal activity before the main brecciation event at Chah Zard. Quartz-adularia, illite, and carbonate–cemented breccias and veins containing fine- to coarse-grained polymetallic sulfide assemblages (pyrite, marcasite, arsenian pyrite, chalcopyrite, sphalerite, galena, and arsenopyrite), silver sulfosalts, electrum, and native gold characterize stage 2. Stage 3 is marked by <1 mm to 5 cm wide crustiform veins of light
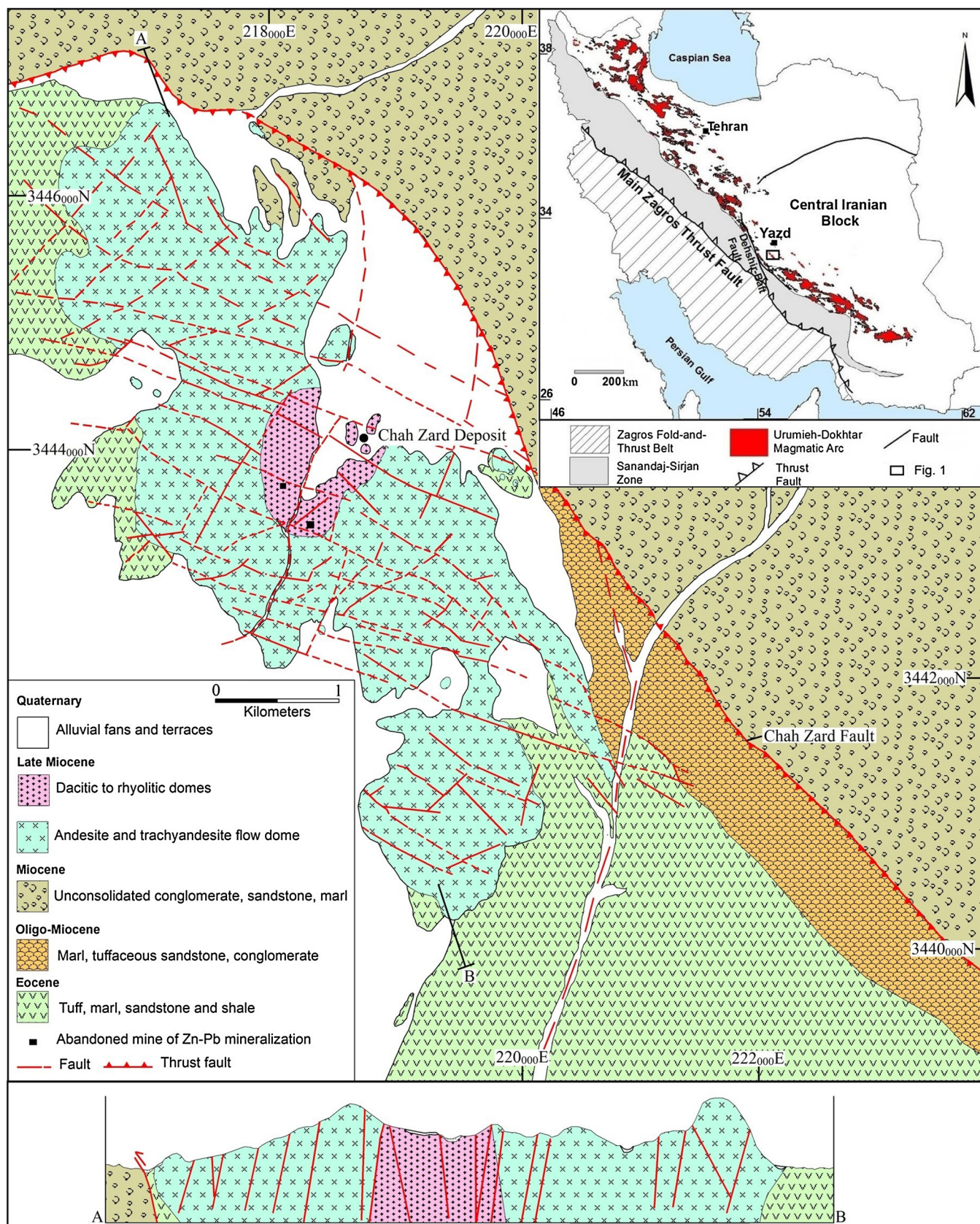
Fig. 1. Geological map of the Chah Zard area (modified from Kouhestani, 2011 and Kouhestani et al., 2012). The insert shows zonal subdivisions of the Zagros orogen (modified from Alavi, 1994) and Dehshir-Baft fault, together with the location of the Chah Zard area in the central part of the UDMA.

Table 1
Summary table describing the main characteristics, pyrite types, and pyrite textures present in each mineralization stages at Chah Zard deposit.

Criteria	Stage 1	Stage 2	Stage 3	Stage 4	Stage 5
Ore mineralogy	Pyrite, minor chalcopyrite	Pyrite, marcasite, arsenian pyrite, chalcopyrite, galena, sphalerite, arsenopyrite, silver sulfosalts, electrum, native gold	Pyrite, marcasite, arsenian pyrite	Pyrite, chalcopyrite, sphalerite, galena, minor electrum	Sphalerite, galena, subordinate pyrite
Alteration assemblages	Quartz, illite	Quartz, adularia, illite, carbonate	Quartz	Quartz, illite, gypsum	Quartz, chlorite, calcite
General occurrences	Vein- veinlet, breccia cements	Vein- veinlet, breccia cements with cockade and plumose textures	Crustiform veins	Vein- veinlet with reovergrown gypsum veins	Vein-veinlet
Pyrite type	Py1	Py2	Py3	Py4	–
Pyrite texture	Medium- to coarse-grained euhedral to subhedral crystals, porous and inclusion-rich, brecciated and rounded shapes are common	Medium- to fine-grained euhedral to subhedral crystals, zoned and rimmed, framboidal, spongy aggregates, fibrous	Coarse-grained euhedral to subhedral crystals, colloform, usually inclusion -free	Subhedral to anhedral crystals, abundant base metal inclusions	–
Gold content of pyrite	Invisible gold Range: <DL to 1 ppm Free gold: none	Invisible gold Range: <DL to 183 ppm Mean: 16 ppm Free gold: common as inclusions	Invisible gold Range: <0.1 to 14 ppm Mean: 1.4 ppm Free gold: may be present as inclusions	Invisible gold Range: <0.3 to 166 ppm Mean: 67 ppm Free gold: common as inclusions	–

DL: detection limit.

gray granular to dogtooth quartz, and colloform pyrite, marcasite, and arsenian pyrite. Stage 4 veins are composed of <1 cm wide quartz veins, with abundant pyrite, chalcopyrite, sphalerite, galena, and subordinate electrum, and traces of tennantite–tetrahedrite, which are re-overgrown by 2 cm wide gypsum veins. Stage 5 occurs as late-stage silver-bearing quartz–sphalerite–galena (±pyrite) veins in peripheral chlorite–calcite alteration areas. Stages 2 and 4 are the most important in terms of gold deposition.

In general, most of the free gold in the Chah Zard deposit occurs as electrum and native gold in pyrite together with chalcopyrite, galena, and sphalerite, with lesser amounts in quartz. The grain size of the gold ranges from <0.05 to 1 mm in diameter and its morphology is variable, ranging from irregularly-shaped, teardrop-like to veinlet forms (Kouhestani, 2011; Kouhestani et al., 2012).

4. Sampling and analytical techniques

Samples for the textural and geochemical study were collected from core drill holes (Fig. 2). A suite of 150 samples were collected and studied from the mineralized zones in the holes to provide a complete spectrum of the mineralogy, textures, and paragenesis at Chah Zard. A selection of the data is presented in Table 2, with sample locations shown in Fig. 2. Mineralogical and textural studies were conducted on 130 thin sections and polished mounts of which 16 were analyzed by LA-ICP–MS for pyrite geochemistry and zonation.

The instrumentations used in this study include high-performance New Wave UP193 and UP213-nm solid-state laser microprobes coupled to Agilent 7500a and 7700x quadrupole mass spectrometers, respectively, at the CODES LA-ICP–MS analytical facility of the University of Tasmania, Hobart, Australia. Analyses were performed in an atmosphere of pure He. The helium gas carrying the ablated aerosol was mixed with Ar immediately after the ablation cell and the mix is passed through a pulse-homogenizing device prior to direct introduction into the torch.

4.1. Quantitative multi-element analysis of pyrite

The quantitative pyrite analyses were performed inline and spot modes. Most analyses were completed along profiles across pyrite grains using a laser beam of 10 μm diameter, a repetition rate of 5 Hz and laser beam energy of 2.5 J/cm^2. In this mode, the data were acquired when the sample was moving with a constant rate of 1–3 μm/s under a fixed beam. The length of profiles was 100–300 μm. The ablating spot sizes varied from 15 to 35 μm in diameter. Smaller spot sizes (down to 10 μm) were used on particularly fine-grained pyrite. Data were collected in the time-resolved mode. The analysis time for each sample was 90 s, comprising a 30-s measurement of background (laser off) and a 60-s analysis with laser on. An integration time of 0.02 s was used for each of the elements measured. The following isotopes were monitored: ^{27}Al, ^{55}Mn, ^{57}Fe, ^{59}Co, ^{60}Ni, ^{65}Cu, ^{66}Zn, ^{75}As, ^{82}Se, ^{95}Mo, ^{107}Ag, ^{109}Ag, ^{111}Cd, ^{115}In, ^{118}Sn, ^{121}Sb, ^{125}Te, ^{182}W, ^{197}Au, ^{202}Hg, ^{205}Tl, ^{208}Pb, ^{209}Bi.

Calibration was performed using an in-house primary standard (STDGL2b-2, Danyushevsky et al., 2003), following the procedure of Longerich et al. (1996) and using Fe as the internal standard. The standard was analyzed twice every one and a half hours to account for the instrument drift, with a 100-μm beam and at 5 Hz. Mass spectrometer drift was <5% between each standard measurement. On this basis, no correction was applied for variations in the Fe internal standard, even when As content of the pyrite was above 5 wt%. The raw analytical data for each analysis was plotted as a line graph and the integration times for background and sample signal selected. The counts are then corrected for instrument drift and converted to concentration values using known values of internal standard. The average cps of four STDGL2b-2 standard analyses was used to calculate the concentration of each measured element in ppm.

All pyrite grains were first examined by reflected light microscopy to avoid free gold grains or other discrete sulfide minerals within the pyrite grains prior to analysis. The objective of these analyses is to obtain the trace element concentrations within pyrite, thus interferences from small inclusions are avoided by closely observing; in the case of sudden count, a correction is made as far as possible by cutting off the 'higher peak'.

4.2. Imaging of pyrite

Imaging was carried out by ablating sets of parallel lines in a grid across the samples. Depending on the sample size, lines were
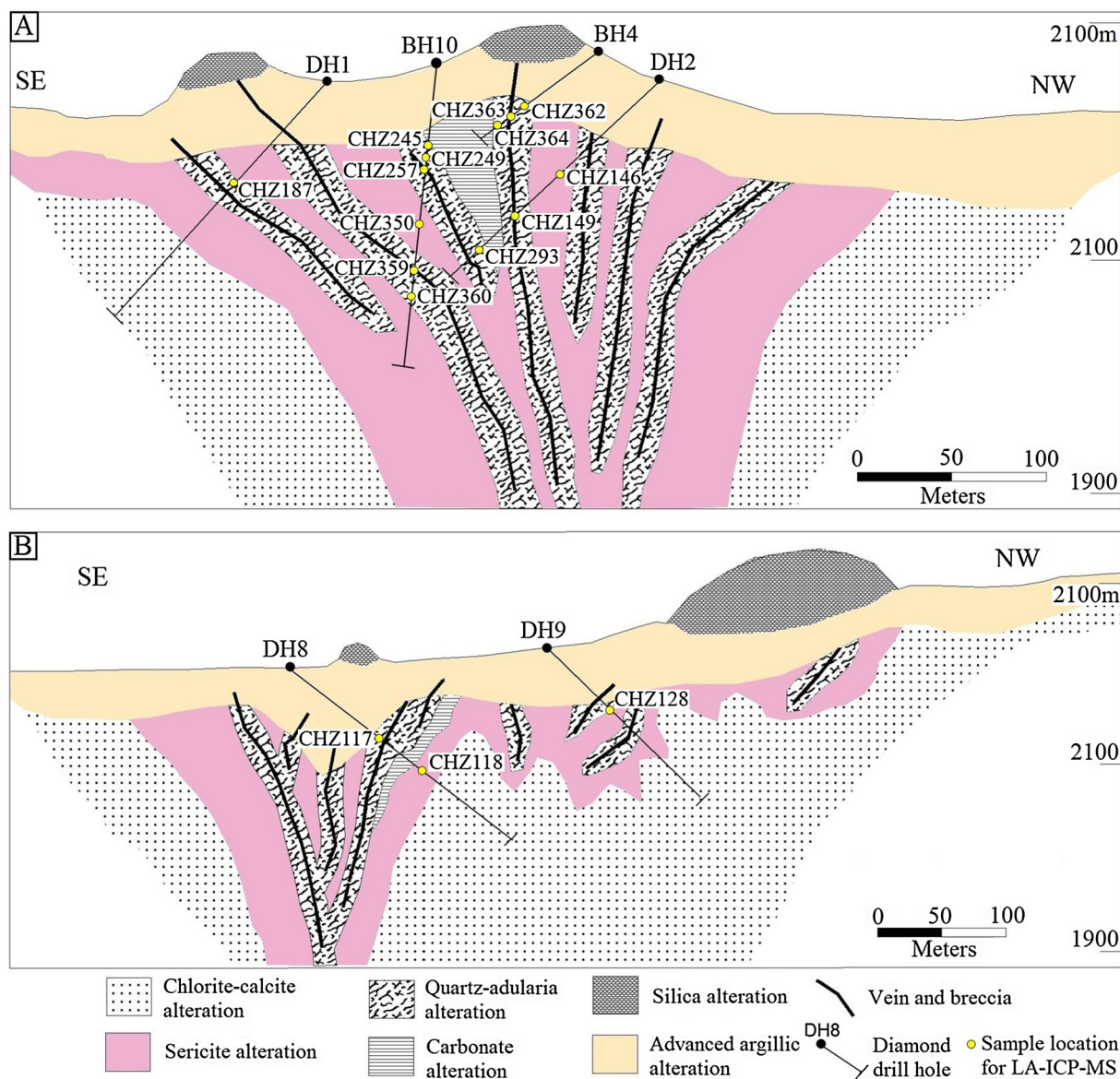
Fig. 2. Generalized geologic sections of Chah Zard, showing the alteration distribution in eastern (A) and western (B) parts of the deposit, and position of the samples selected for this study (after Kouhestani et al., 2012).

ablated with a beam size of 4 or 6 μm. The spacing between the lines was kept constant at the same size as the laser beam. The lines were ablated with the repetition rate of 10 Hz, thus, every position in the sample was ablated 10 times and its composition contributed to 5 consecutive pixels in the image, resulting in an unprocessed effective resolution matching the beam size. Every sweep recorded in the mass spectrometer forms a separate pixel in the map. For a normal sweep time of ∼0.2 s, with an image speed of 25 μm/s, one pixel equals 5 μm.

Depth of ablation during mapping was around 5 μm. A set of 22 elements, including ^{27}Al, ^{55}Mn, ^{57}Fe, ^{59}Co, ^{60}Ni, ^{65}Cu, ^{66}Zn, ^{75}As, ^{82}Se, ^{95}Mo, ^{109}Ag, ^{111}Cd, ^{115}In, ^{118}Sn, ^{121}Sb, ^{125}Te, ^{182}W, ^{197}Au, ^{202}Hg, ^{205}Tl, ^{208}Pb, and ^{209}Bi were analyzed with acquisition time for masses set to 0.002 s. The total sweep time was ∼0.2 s. To allow for cell wash-out, a delay of 13 s was used after each line. Background levels and the primary sulfide standard (STDGL2b-2, Danyushevsky et al., 2003) were measured before and after each image. Detailed processing for the laser imaging technique and data reduction are the same as described in Large et al. (2009).

5. Textural features of pyrite

Pyrite is the predominant sulfide mineral in all mineralization stages at Chah Zard. Visual examination and petrographic observation combined with scanning electron microscopy-backscattered electron images suggest a variety of pyrite types in the paragenetic sequence, marked by distinct morphology, textures, and mineral associations. Stage 1 pyrite (py1) is typically porous and gold-poor. It is present as medium- to coarse-grained (<1 to several mm in size), euhedral to subhedral disseminated grains with cubic or pyritohedral forms or as aggregate masses in pyrite-rich veins. The pyrite generally appears fractured, leaving behind several 0.2–0.5 mm wide brecciation zones that are usually not filled with other sulfide minerals (Fig. 3a). Some grains are characterized by well-rounded shapes (Fig. 3b); which may indicate hydrothermal transport during the ore genesis.

Pyrite from stage 2 (py2) occurs as disseminations, veins or veinlets, and massive accumulations in hydrothermally cemented breccias. Disseminated crystals are dominated by medium- to

Table 2
Summary table describing the samples selected for LA-ICP–MS.

Sample No.	Drill hole	Description	Ore mineralogy	Alteration assemblage	Pyrite type and texture
CHZ117	DH8	Matrix-supported monomictic breccia	Pyrite	Quartz, illite	Brecciated py1
CHZ118	DH8	Clast- to matrix-supported monomictic breccia	Pyrite	Illite, minor chlorite and calcite	Brecciated and rounded py1
CHZ128	DH9	Rhyolite porphyry with calcite-pyrite veinlets	Pyrite, minor chalcopyrite	Illite, calcite	Fibrous py2
CHZ146	DH2	Matrix-supported polymictic breccia	Pyrite	Quartz, illite	Well-rounded porous py1
CHZ149	DH2	Clast-supported polymictic breccia with quartz- adularia cement	Pyrite, arsenian pyrite, chalcopyrite, electrum	Quartz, adularia, illite	Simple-zoned py2
CHZ187	DH1	Clast-supported polymictic breccia with quartz cement	Pyrite, minor chalcopyrite	Quartz, illite	Well-rounded porous and inclusion-rich py1
CHZ245	BH10	Clast-rotated polymictic breccia with quartz- adularia and sulfide cement	Pyrite, arsenian pyrite, galena, sphalerite, chalcopyrite, arsenopyrite, silver sulfosalts	Quartz, adularia, illite	Simple-zoned py2
CHZ249	BH10	Clast-supported matrix-rich polymictic breccia with crustiform quartz-sulfide veins	Pyrite, marcasite, arsenian pyrite	Quartz, illite	Colloform py3
CHZ257	BH10	Clast-rotated polymictic breccia with quartz and sulfide cement	Pyrite, marcasite, chalcopyrite, arsenian pyrite	Quartz, illite	Simple-zoned and oscillatory-rimmed py2
CHZ293	DH2	Clast-supported matrix-rich polymictic breccia	Pyrite, chalcopyrite	Quartz, illite	Framboidal py2
CHZ350	BH10	Matrix-supported polymictic breccia	Pyrite, marcasite, chalcopyrite, arsenian pyrite, arsenopyrite	Quartz, illite	Fibrous and simple-zoned py2
CHZ359	BH10	Clast-supported matrix-rich polymictic breccia with crustiform quartz-sulfide veins	Pyrite, marcasite, arsenian pyrite	Quartz, illite, minor adularia	Colloform py3
CHZ360	BH10	Clast-rotated polymictic breccia with quartz- adularia and sulfide cement	Pyrite, marcasite, chalcopyrite, arsenian pyrite, galena	Quartz, illite	Brecciated py1, simple-zoned and oscillatory-rimmed py2
CHZ362	BH4	Clast-rotated polymictic breccia with quartz- adularia and sulfide cement	Pyrite, chalcopyrite, sphalerite, galena, electrum	Quartz, adularia, illite	Inclusion-rich py4
CHZ363	BH4	Clast-rotated polymictic breccia with quartz- adularia and sulfide cement	Pyrite, chalcopyrite, sphalerite, galena, electrum	Quartz, adularia, illite	Inclusion-rich py4
CHZ364	BH4	Clast-rotated polymictic breccia with quartz- adularia and sulfide cement	Pyrite, chalcopyrite, sphalerite, galena, electrum	Quartz, adularia, illite	Inclusion-rich py4

fine-grained euhedral to subhedral grains ranging in size from several μm to 2 mm. They are in many cases surrounded by arsenian pyrite and marcasite/pyrite showing zonation (Fig. 3c). In some parts of the deposit, subhedral to euhedral pyrites have chalcopyrite and galena as inclusions and in its surroundings (Fig. 3d). Visible gold grains occur intergrown with pyrite. Some free gold inclusions were found in the disseminated porous coarse-grained (usually 3–8 mm in size) anhedral pyrite (Fig. 3e). Pyrite veins and veinlets occur in subparallel sheeted to stockwork sets, or as isolated elongate wisps and tension gashes, and have crosscutting relationships with py1. Typically individual veins and veinlets are laterally discontinuous, but the vein-veinlet sets are persistent, and consistently oriented for several meters. The veins commonly show evidence of multiple reopening events that are generally sealed by arsenian pyrite and/or marcasite (Fig. 3f). No visible gold was identified either in hand specimen or under the microscope from pyrite veins and veinlets; however the veins are commonly associated with ore-grade mineralization. The pyrite veins and veinlets are transitional to base-metal sulfides and sulfosalts–dominated veins. Based on optical and scanning electron microscopy-backscattered electron observations, four textural styles of py2 are recognized: simple-zoned, oscillatory-rimmed, framboidal and "fibrous" pyrites. Both simple-zoned and oscillatory-rimmed pyrites consist of a mineral inclusion-rich core and inclusion-free rim; however, in oscillatory-rimmed pyrite, the latter is composed of complex rhythmic overgrowths of alternating As-rich and As-poor bands. Framboidal pyrite displays typical framboid textures of pyrite microcrystals in spheres from 0.01 to 0.05 mm across (Fig. 4a), and fibrous pyrite is composed of needle-shaped pyrite crystals deposited over rhombic and bladed carbonate (Fig. 4b).

Stage 3 pyrite (py3) occurs in quartz vein-hosted colloform sulfide vein (pyrite 75 vol.%, marcasite 20 vol.%, and arsenian pyrite 5 vol.%) (Fig. 4c, d). Pyrite is characterized by euhedral to subhedral

grains, and is usually inclusion-free. The stage 4 pyrite (py4) is commonly intergrown with other sulfide minerals including chalcopyrite, galena, and sphalerite and characterized by subhedral to anhedral crystals of 0.05 mm to 2 cm across (Fig. 4e). The py4 may also contain inclusions of sphalerite and other sulfide minerals, and inclusions of free gold. Abundant visible gold grains (up to 1 mm in diameter) are found as intergrown with pyrite and quartz (Fig. 4f). Pyrite from stages 2 and 4 is the main host for gold. Bulk chemical analyses of mineralized veins and breccias (Kouhestani, 2011) also yielded high gold values of 17.8 and 66.5 ppm in samples containing py2 and py4, respectively.

6. LA-ICP–MS trace element geochemistry of pyrite

The trace element geochemistry of the various pyrite types was determined by LA-ICP–MS on a suite of 16 representative samples through the mineralized zone. Table 3 gives representative analyses of each pyrite type. Figs. 5 and 6 show, respectively, selected laser line and spot analyses for gold and silver in typical types of pyrite, and Fig. 7 shows gold concentration ranges in each pyrite type.

Py1 contains a wide range of trace elements, the most abundant of which are As, Cu, Pb, Zn, Ag, and Sb. Transition metals Co and Ni have high concentrations on the order of tens of hundreds of ppm to less than 100 ppm. Copper, Pb and Zn have concentrations of tens to hundreds of ppm. Thallium and Bi concentrations from py1 grains at Chah Zard are generally <4 ppm and average concentrations are less than 1 ppm. Molybdenum and Sn values, respectively, range from below detection to 7 and 4 ppm. Tungsten and Te values are mostly concentrated at levels of below detection. Antimony ranges from 5 to 100 ppm. The invisible gold is mostly concentrated at levels of <1 ppm (one rounded pyrite grain recorded 6 ppm Au) to below detection. Silver and As are more
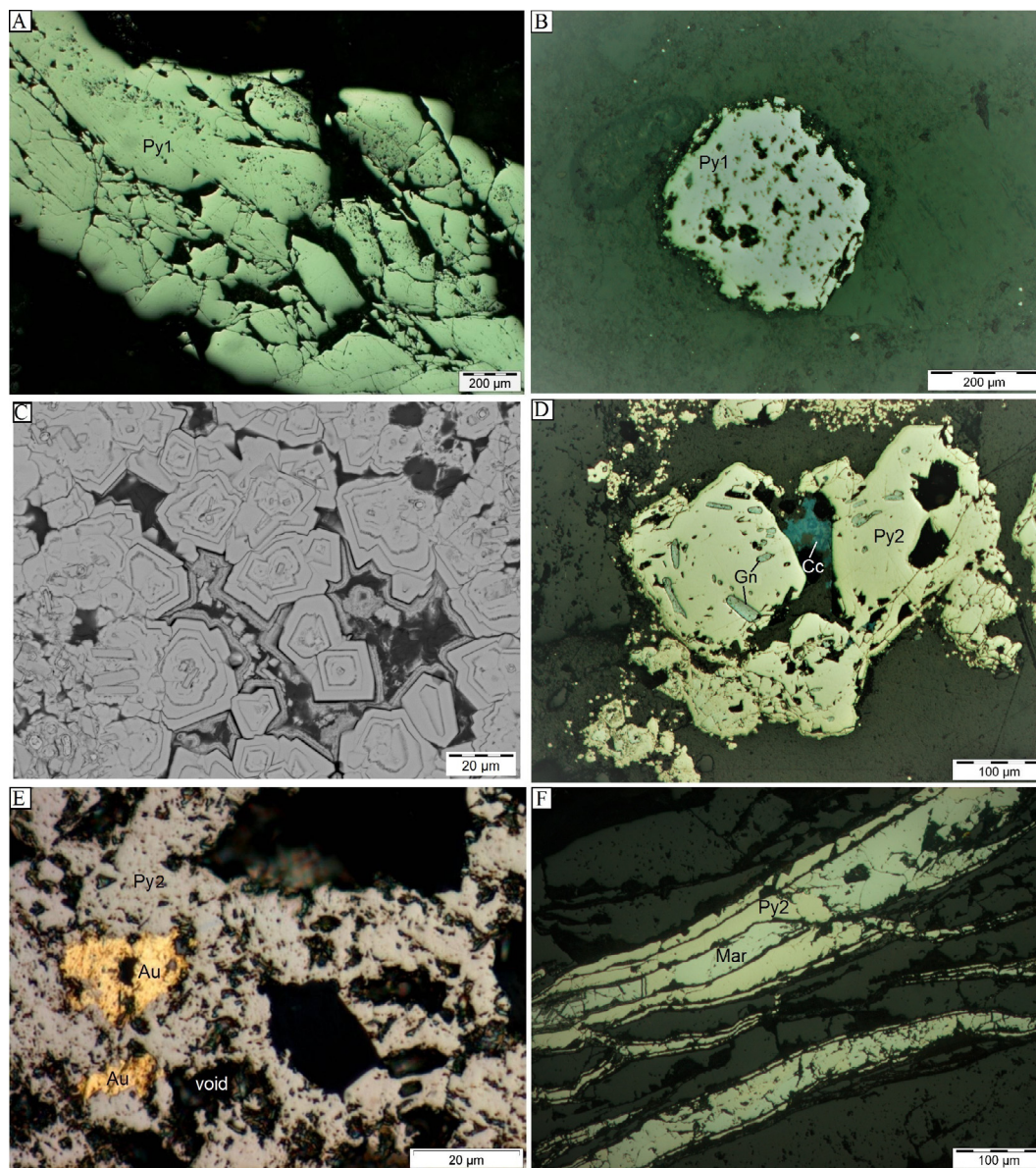
Fig. 3. Reflected-light photomicrographs and backscattered electron (BSE) image showing textures of pyrite types at Chah Zard. A. Vein of py1 which was generally fractured by brecciation zones. B. Well-rounded porous py1 grain. C. Euhedral to anhedral simple-zoned and oscillatory-rimmed py2, etched with nitric acid, surrounded by arsenian pyrite. D. Galena occurs as inclusions in subhedral coarse-grained py2. Chalcopyrite (replaced by chalcocite) occurs as fracture-filling in py2. E. Gold occurs as inclusions in porous anhedral py2. F. Subparallel sheeted py2 veins sealed by marcasite. *Apy*: *arsenian pyrite*, *Au*: *gold*, *Cc*: *chalcocite*, *Cpy*: *chalcopyrite*, *F-Py*: *framboidal pyrite*, *Gn*: *galena*, *Mar*: *marcasite*, *Py*: *pyrite*, *Qtz*: *quartz*, *Sph*: *sphalerite*, *S-Py*: *spongy pyrite*.

anomalous than Au with detectable Ag and As occurring in all grains ranging from 10 to 1516 ppm (mean = 119 ppm Ag) and 47 to 23,413 ppm (mean = 4717 ppm As), respectively. Detailed LA-ICP–MS analysis of the py1 grains indicates that they are commonly enriched in submicroscopic inclusions of Ag-Au tellurides. Typically, the rims of disseminated pyrites are enriched in Au and As, and depleted in Ag compared to the cores (Table 3). A LA-ICP–MS output trace for well-rounded py1 is shown in Fig. 5a. The spiky pattern for the counts of Au, Ag, and Te indicate that these pyrite grains contain small amounts of Au–Ag-bearing tellurides, occurring as submicroscopic inclusions or solid solutions. Although arsenic is present in these grains, gold is lacking. Weak positive correlations between Au–As and Au–Sb, and negative correlation between Au–Cu are evident in the disseminated py1 data (Fig. 8a–d).

Compared with py1, py2 is enriched in most trace elements (Table 3). The invisible gold content of py2 varies from below

detection to 162 ppm (mean = 16 ppm Au), and Ag and As, respectively, varies from 0.6 to 3841 ppm (mean = 673 ppm Ag) and 50 to 73,150 ppm (mean = 26,367 ppm As). Simple-zoned pyrite has the highest levels of gold of all the py2 grains (Table 3). These high gold analyses are most likely due to inclusions of free gold within the simple-zoned pyrite that have been sampled by the laser (e.g., Large et al., 2007). Fig. 8e–l illustrates the correlations between Au, Ag, As and other trace elements in rimmed py2. The marked enrichment of Au in inner rims compared with cores and outer rims is displayed in Fig. 6e. There is a negative correlation between Au-Ag, Au-Sb and Au-Cu in the inner rims, but a positive correlation between Au and these elements are evident in outer rims. There is negative correlation between Au and Mo, but a positive correlation between Au, As, Pb and Ni is noticed. Tellurium shows weak positive correlation with Au (Fig. 8j) indicating that invisible gold occurred as submicroscopic inclusions of Au tellurides. The LA-ICP–MS profile for rimmed py2 (Fig. 5b) is marked
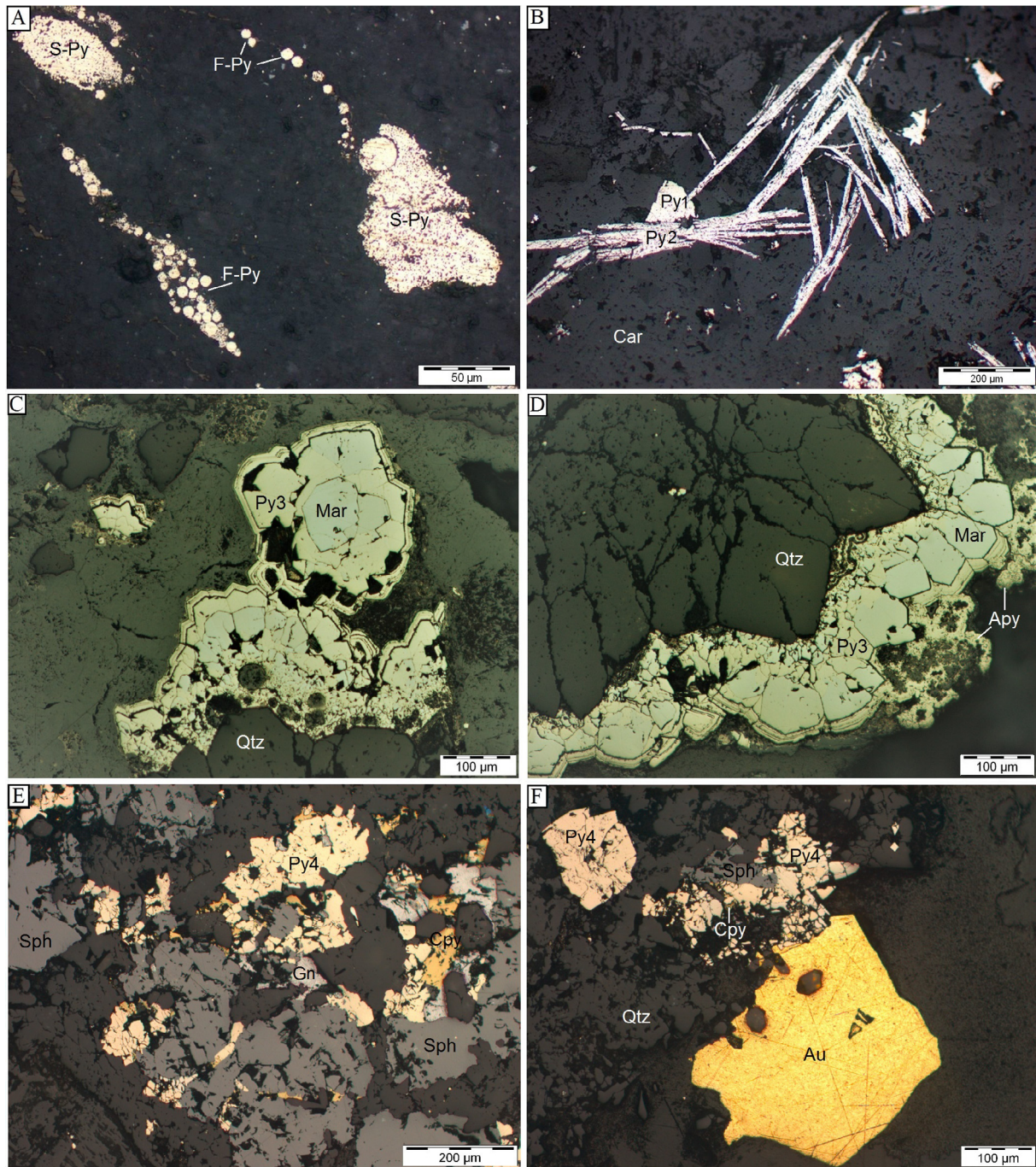
Fig. 4. Reflected light photomicrographs showing textures of pyrite types at Chah Zard. A. Clusters of py2 framboids. Framboidal pyrite commonly coalesces into large mats of spongy pyrite. B. Fibrous py2. C and D. Colloform py3 in quartz vein. E. Anhedral py4 intergrown with galena, sphalerite and chalcopyrite. F. Free gold intergrown with py4 which is intergrown with sphalerite and chalcopyrite. Abbreviations as in Fig. 3.

by very high gold concentrations in the inner rims, possibly hundreds of ppm Au. There are also high concentrations of Te, with spectra constantly parallel to those of Au. This is best interpreted as presence of inclusions of Au–Te assemblages (e.g., Bi et al., 2011). Silver concentrations are generally very high in the outer rims. Spikes in the LA-ICP–MS trace for Ag, As, and Sb indicate the presence of submicroscopic inclusions of a mineral (e.g., Ag–sulfosalts) containing these elements (e.g., Large et al., 2007). Representative framboidal py2 yield Au, and Te concentrations that are comparable to the respective background values, with Ag being slightly higher than the background (Fig. 5c). This suggests that

the framboidal pyrite contains very little Au, Te, and Ag. The fairly flat pattern for the counts of all the elements listed (Pb, Co, As, Sb, Bi, Ag, Te, and Au) and their similar pattern to the Fe counts suggest that these elements are most probably restricted within the structure of the pyrite (e.g., Large et al., 2007).

Py3 in the colloform sulfide veins is depleted in most trace elements (excluding As which has a significantly higher content and varies from 1516 to 121,295 ppm; mean = 22,071 ppm As) compared to py2. The concentration of invisible gold varies from <0.12 to 14 ppm (mean = 1.4 ppm Au), and silver varies from <0.1 to 367 ppm (mean = 86 ppm Ag) (Table 3). Tellurium values are mostly

Table 3
Selected LA-ICP–MS analyses of different pyrite types from Chah Zard deposit.

Analysis No.	Pyrite type	Au (ppm)	Ag (ppm)	Mn (ppm)	Fe (ppm)	Co (ppm)	Ni (ppm)	Cu (ppm)	Zn (ppm)	As (ppm)	Mo (ppm)	Sn (ppm)	Sb (ppm)	Te (ppm)	W (ppm)	Tl (ppm)	Pb (ppm)	Bi (ppm)
SE06A034	Py1 DC	<0.1	89	<2	465,000	8	301	1233	440	188	<0.3	<0.6	130	<1	0.3	0.2	474	1
	Py1 DR1	0.5	43	2	465,000	125	451	886	112	12,503	<0.2	<0.5	89	<1	<0.2	0.3	513	3
	Py1 DR2	<0.2	10	4	465,000	0.3	100	171	<9	47	<0.4	<0.8	10	<2	<0.3	1	52	<0.2
SE06A037	Py1 DC	<0.1	24	<2	465,000	<0.1	<1	1721	873	340	<0.3	<0.5	104	<1	<0.3	0.4	571	<0.5
	Py1 DR1	0.6	19	<1	465,000	12	23	889	134	12,511	7	<0.4	101	<1	<0.2	1	425	<0.4
	Py1 DR2	<0.2	16	1	465,000	0.1	6	53	<7	52	1	1	5	<1	0.3	2	34	<0.7
SE06A038	Py1 DC	<0.2	137	2	465,000	5	16	1780	391	4821	<0.4	0.3	255	<2	<0.4	1	1320	1
	Py1 DR1	0.6	35	2	465,000	22	55	507	553	23,413	3	1	59	<1	0.2	1	295	1
	Py1 DR2	0.1	31	7	465,000	10	54	345	13,383	3114	<0.4	4	36	<2	<0.4	2	148	0.2
SE06A035	Py1 V	0.2	19	13	465,000	13	38	358	109	8288	<0.3	<0.5	47	<1	<0.3	0.2	128	<0.8
		0.3	47	3	465,000	17	92	267	72	7136	<0.3	1	73	<1	<0.3	2	394	3
SE06A036	Py1 V	0.1	13	2	465,000	9	99	98	9	2705	<0.3	<0.9	16	1	<0.4	1	65	0.3
SE06A003	Py2 RC	2	39	<4	465,000	142	1149	403	<13	3104	<0.6	<1	20	38	<0.6	32	43	1
	Py2 RR1	25	1225	51	465,000	736	1341	19,019	64	36,067	11	1	360	23	8	924	301	0.4
	Py2 RR2	1	2319	52	465,000	1283	1674	70,574	504	57,621	25	2	1069	2	7	2632	426	<0.5
SE06A004	Py2 RC	4	54	<3	465,000	114	860	428	<11	3672	<0.5	<1	25	111	<0.5	36	44	1
	Py2 RR1	20	661	197	465,000	407	1043	8879	45	24,491	6	<0.7	207	23	446	632	178	2
	Py2 RR2	4	840	257	465,000	529	411	17,600	107	33,036	10	0.2	363	3	1132	1238	182	1
SE06A005	Py2 RC	2	172	259	465,000	343	2591	194	<8	6339	1	<0.9	44	135	1	14	177	2
	Py2 RR1	22	412	68	465,000	401	1690	3221	21	14,527	12	<0.7	200	46	244	254	250	3
	Py2 RR2	1	2235	130	465,000	1468	1605	65,305	601	54,295	28	<2	899	12	12	2776	444	<0.4
SE06A006	Py2 RC	1	1357	191	465,000	772	700	33,389	265	39,960	14	<0.9	409	6	12	1497	204	<0.2
	Py2 RR1	11	1257	177	465,000	650	914	23,237	182	37,602	12	<0.6	383	24	17	1273	251	0.3
	Py2 RR2	2	1720	151	465,000	1037	958	40,637	373	46,379	19	<1	626	10	48	2059	340	<0.3
SE06A007	Py2 RC	<0.3	3	51	465,000	2	386	59	<7	50	<0.3	<0.7	2	<1	<0.4	5	13	<0.1
	Py2 RR1	12	771	169	465,000	346	570	16,509	139	27,030	6	<0.7	211	8	7	702	139	<0.2
	Py2 RR2	1	3841	98	465,000	2843	23,265	31,569	129	73,150	8	0.1	5471	1	8	8535	154	0.2
SE06A008	Py2 RC	7	185	22	465,000	270	2167	827	<12	11,122	<0.6	<1	73	50	1	73	167	1
	Py2 RR1	19	511	145	465,000	262	995	4475	27	30,294	3	<0.6	168	24	4	546	129	0.3
	Py2 RR2	1	1680	215	465,000	846	850	38,835	310	41,578	15	<0.9	318	8	16	1608	217	<0.2
SE06A009	Py2 RC	0.2	441	195	465,000	162	136	4828	24	26,702	2	<1	41	2	12	280	47	<0.3
	Py2 RR1	2	1038	202	465,000	538	516	17,699	93	32,623	9	<0.8	214	10	24	771	200	<0.2
	Py2 RR2	3	761	231	465,000	387	337	11,214	52	32,009	6	<0.8	174	7	17	680	172	<0.2
SE06A010	Py2 RC	0.3	431	259	465,000	85	68	3170	26	31,790	1	<1	83	1	26	424	41	<0.2
	Py2 RR1	2	748	300	465,000	285	232	10,639	67	35,667	5	<0.8	276	4	42	823	137	<0.2
	Py2 RR2	1	1643	431	465,000	825	793	54,039	1273	46,475	15	<1	1036	10	48	1897	432	<0.3
SE06A011	Py2 RC	0.2	558	293	465,000	214	165	8720	84	31,081	4	<1	189	2	19	601	58	<0.3
	Py2 RR1	7	1089	332	465,000	523	488	29,201	481	40,458	9	<1	592	6	26	1160	253	<0.3
	Py2 RR2	1	1507	762	465,000	754	893	62,757	2910	46,282	13	<2	1165	12	258	1617	768	<0.7
SE06A012	Py2 RC	<0.4	309	244	465,000	56	62	2811	27	27,164	1	<1	40	<2	10	229	29	<0.2
	Py2 RR1	2	1025	294	465,000	456	478	18,648	180	36,909	7	0.3	422	6	30	980	232	<0.2
	Py2 RR2	<2	2031	1601	465,000	1106	1649	106,654	7891	57,410	19	<6	3459	9	20	2507	2057	<1
SE06A043	Py2 ZC	3	18	116	465,000	825	396	75	14	5510	1	1	127	2	3	392	423	20
	Py2 ZR1	156	64	99	465,000	544	3330	350	18	42,799	2	1	327	<2	4	2004	246	0.2
	Py2 ZR2	6	56	276	465,000	425	1879	37	21	29,078	1	<0.7	260	<2	3	2421	210	<0.2
SE06A045	Py2 ZC	<0.2	1	0.4	465,000	55	1279	6	<7	449	0.2	<0.6	2	<2	<0.4	0.3	8	0.3
	Py2 ZR1	140	41	7	465,000	278	2240	571	9	29,307	2	<0.6	211	<2	2	803	263	<0.2

Table 3 (*continued*)

Analysis No.	Pyrite type	Au (ppm)	Ag (ppm)	Mn (ppm)	Fe (ppm)	Co (ppm)	Ni (ppm)	Cu (ppm)	Zn (ppm)	As (ppm)	Mo (ppm)	Sn (ppm)	Sb (ppm)	Te (ppm)	W (ppm)	Tl (ppm)	Pb (ppm)	Bi (ppm)
SE06A046	Py2 ZC	2	1	<2	465,000	47	332	33	<7	309	<0.3	1	16	<2	<0.3	2	89	0.3
	Py2 ZR1	45	5	8	465,000	89	804	175	<9	9513	0.5	<0.7	46	<3	0.5	74	61	0.3
SE06A047	Py2 ZC	0.4	2	8	465,000	45	228	43	<8	710	1	<1	33	2	3	2	194	1
	Py2 ZR1	162	8	4	465,000	124	858	486	<7	18,159	1	<0.7	67	<2	1	112	848	1
SE06A068	Py2 ZC	0.2	132	33	465,000	1	58	15	<5	208	<0.3	<0.6	6	12	0.3	2	3862	6
	Py2 ZR1	20	721	223	465,000	23	261	2263	5	8967	0.1	0.2	1016	4	1446	432	198	0
	Py2 ZR2	5	748	716	465,000	125	295	4227	51	27,477	3	0.2	904	5	3048	1350	320	<0.3
SE06A069	P Py2 ZC	0.4	27	1300	465,000	3	549	32	<6	221	0.4	<0.6	16	2	0.2	5	187	0.1
	Py2 ZR1	32	649	971	465,000	54	260	1949	280	16,250	1	1	812	27	1060	326	292	0.2
	Py2 ZR2	2	569	474	465,000	115	229	5787	64	45,890	5	1	1075	10	1038	1746	354	<0.2
SE06A013	Py2 V	6	1295	328	465,000	690	807	31,958	143	29,167	10	0.2	472	15	472	1458	170	1
SE06A014	Py2 V	17	1508	608	465,000	675	1378	196,448	1438	45,612	16	19	873	6	45	3377	1892	6
SE06A052	Py2 V	0.2	2	749	465,000	6	34	19	170	20,876	1	0	186	0	44	170	42	<0.3
SE06A053	Py2 V	0.3	3	775	465,000	5	26	15	102	12,583	1	<0.7	135	<2	42	124	36	0.1
SE06A054	Py2 V	0.4	221	890	465,000	27	122	93	383	54,009	5	<1	675	<3	1059	560	99	0
SE06A055	Py2 V	0.2	98	939	465,000	19	107	70	292	58,841	4	1	600	<3	489	445	113	<0.3
SE06A060	Py2 F	2	20	16	465,000	1580	2437	88	78	2322	3	<1	151	35	42	2	514	42
SE06A061	Py2 F	1	13	42	465,000	2094	3189	125	218	2859	9	<3	146	30	<3	7	305	32
SE06A062	Py2 F	1	8	14	465,000	787	1998	95	51	3025	2	<0.6	99	15	<0.4	3	187	21
SE06A063	Py2 F	1	27	51	465,000	2302	3414	318	3407	3776	10	<3	158	41	4	6	491	43
SE06A020	Py3 CC	<0.2	12	3975	465,000	3	5	19	60	8910	1	<0.6	40	<1	978	310	1	<0.1
	Py3 CR1	0.1	18	4191	465,000	8	16	32	89	14,705	1	<0.6	41	<1	747	678	2	<0.2
	Py3 CR2	1	76	2726	465,000	24	65	100	125	24,423	2	0.2	131	<2	520	1551	7	0
SE06A021	Py3 CC	<0.24	35	2710	465,000	54	114	91	120	16,437	2	0.5	124	<2	1637	422	8	0.1
	Py3 CR1	0.1	28	4129	465,000	16	33	68	104	15,292	1	0.2	69	<2	837	869	3	0.1
	Py3 CR2	0.2	40	3381	465,000	14	36	52	102	19,703	1	0.4	68	<1	614	1187	3	0.1
SE06A022	Py3 CC	6	124	688	465,000	55	131	236	115	42,239	2	1	121	3	65	707	11	0.2
	Py3 CR1	0.4	58	3182	465,000	15	38	42	94	23,747	1	<073	83	<2	515	1097	3	<0.2
	Py3 CR2	14	253	2966	465,000	188	582	365	544	63,877	8	0.4	740	3	945	1340	54	0.2
SE06A023	Py3 CC	1	288	1352	465,000	88	134	161	189	24,445	2	<0.9	138	<2	245	571	12	<0.2
	Py3 CR1	0.2	49	2955	465,000	11	28	36	76	17,798	1	<0.7	67	<2	955	635	6	0
	Py3 CR2	5	367	2561	465,000	79	239	321	354	55,900	10	0.3	588	2	896	1417	74	0.2
SE06A024	Py3 CC	<0.1	0.5	2293	465,000	<0.1	0.4	3	16	1861	<0.2	<0.4	0.2	<1	9463	5	0.2	<0.1
	Py3 CR1	0.1	17	4340	465,000	7	15	21	48	5037	1	0.1	32	<1	863	103	2	0
	Py3 CR2	3	229	2786	465,000	58	187	365	212	31,129	5	1	349	<1	546	1486	15	<0.2
SE06A025	Py3 CC	<0.1	<0.1	2264	465,000	<0.1	<0.4	<0.5	14	1516	<0.2	<0.4	<0.2	<1	10,713	3	0	<0.1
	Py3 CR1	<0.2	7	4265	465,000	7	12	8	48	4419	1	<0.6	28	<1	4233	78	148	<0.2
	Py3 CR2	<0.3	4	5152	465,000	3	23	<1	59	5282	1	<0.8	10	<2	718	105	3	<0.2
SE06A026	Py3 CC	<0.3	<0.2	4934	465,000	<0.1	<0.7	<0.8	<7	2701	1	<0.7	1	<2	3781	0	<0.1	<0.2
	Py3 CR1	<0.2	7	5102	465,000	1	4	19	60	6214	1	<0.5	29	<2	2385	183	0.4	<0.1
	Py3 CR2	2	129	3529	465,000	28	85	424	182	19,173	3	<0.6	207	<2	1831	924	9	0.1
SE06A027	Py3 CC	<0.2	1	2605	465,000	0.4	1	1	32	4179	<0.3	<0.6	2	<1	3361	2	0.2	<0.1
	Py3 CR1	0.1	29	4210	465,000	3	7	47	53	6128	1	<0.5	35	0.1	2012	280	1	<0.1
	Py3 CR2	2	106	3120	465,000	24	104	295	218	21,838	3	0.2	234	<1	2147	885	58	<0.1
SE06A028	Py3 CC	<0.3	98	2223	465,000	41	75	124	73	13,695	1	<0.7	95	2	581	446	4	<0.2
	Py3 CR1	0.2	42	3312	465,000	4	6	11	57	18,202	1	<0.5	31	<1	579	907	0.3	<0.1
	Py3 CR2	2	189	2453	465,000	25	101	139	138	36,195	2	0.2	199	1	509	1919	7	<0.1
SE06A029	Py3 CR1	0.2	21	4633	465,000	3	4	4	90	13,721	1	<0.5	32	<1	685	879	0.2	<0.1

Table 3 (continued)

Analysis No.	Pyrite type	Au (ppm)	Ag (ppm)	Mn (ppm)	Fe (ppm)	Co (ppm)	Ni (ppm)	Cu (ppm)	Zn (ppm)	As (ppm)	Mo (ppm)	Sn (ppm)	Sb (ppm)	Te (ppm)	W (ppm)	Tl (ppm)	Pb (ppm)	Bi (ppm)
	Py3 CR2	3	277	1615	465,000	147	494	216	426	121,295	8	0.4	674	1	574	6155	24	<0.1
SE28A60	Py4	<0.2	421	4	465,000	<0.6	<2	632	276	547	<0.4	<2	1374	<4	0	5	1109	0.5
SE28A61	Py4	46	1152	1	465,000	0.4	2	2420	95	9201	<0.1	<0.4	1668	13	<0.2	11	1946	1
SE28A62	Py4	27	4973	3	465,000	10	13	1133	208	7925	0.3	<0.6	2590	6	<0.1	24	959	1
SE28A63	Py4	4	1842	2	465,000	0.3	37	1282	507	1322	<0.3	<0.5	2207	16	<0.2	5	1629	3
SE28A65	Py4	2	639	4	465,000	4	10	4810	155	5008	0.5	<0.5	1541	16	0.1	49	668	0.3
SE28A66	Py4	166	1301	3	465,000	0.4	358	1463	61	10,223	0.2	0.4	516	13	0	253	7641	1
SE28A67	Py4	142	397	3	465,000	3	443	330	64	76,047	0	0.4	869	71	0	35	2934	0.2
SE28A68	Py4	88	890	140	465,000	3	1455	8593	1233	23,479	0	1	941	31	3	89	3081	1
SE28A69	Py4	128	575	28	465,000	3	750	2190	66	34,658	0	0.3	519	27	18	111	3445	0.2

DC: disseminate-core, DR1: disseminate-inner rim, DR2: disseminate-outer rim, V: vein, RC: oscillatory-rimmed-core, RR1: oscillatory-rimmed-inner rims, RR2: oscillatory-rimmed-outer rims, ZC: simple-zoned-core, ZR1: simple-zoned-inner rim, ZR2: simple-zoned-outer rim, F: framboidal, CC: colloform-core, CR1: colloform-inner rim, CR2: colloform-outer rim.

concentrated at levels below detection, indicating that Au in py3, when present, occurs as invisible gold or electrum (e.g., Bi et al., 2011). The marked contrast in trace element content between inner and outer rims of py3 is shown in Fig. 9, which represents an enrichment of Au, Ag, and most other trace elements in the outer rims. Although minor amounts of Au, and Ag were detected in the inner rims, there is a positive correlation between these elements in the outer rims (Fig. 9a). The positive correlation for Au-Cu, Au-Zn, and Au-Pb (Fig. 9d–f) as well as Ag-Sb and Ag-Pb is likely due the abundant submicroscopic inclusion of chalcopyrite, sphalerite, galena and silver sulfosalts. LA-ICP–MS output for Au, Ag, as well as Sb, Cu, and Pb, is generally ragged, suggesting the overall presence of submicron inclusions in the ablated material (Fig. 5d). Virtually no Te was detected for this ablation. The laser ablation profile is marked by below background values of Au in porous cores. In contrast, void-free rims yielded Au concentrations, about one to two magnitudes higher than the background values.

Py4 is commonly intergrown with other sulfide minerals and contains microscopic inclusions of galena, sphalerite, chalcopyrite, and free gold, which contribute to the complexity of the trace element patterns. Due to these inclusions, it was not possible to obtain a pure laser line analysis on this type of pyrite. A laser beam diameter of 10–35 μm was commonly used to analyze py4 grains. LA-ICP–MS spot analysis of the py4 indicates that it is relatively enriched in all trace elements except Mo, Sn, and W (Table 3). The invisible gold values vary from <0.2 to 166 ppm (mean = 67 ppm Au) and silver and arsenic contents, respectively, range from 397 to 4973 ppm (mean = 1354 ppm Ag) and 547 to 76,047 ppm (mean = 18,712 ppm As).

7. Composition and zonation of pyrite

The pyrite samples mapped by LA-ICP–MS for this study were selected from py1, py2 and py3. No samples were selected from py2 framboids and py4 grains, respectively, due to the fine-grained nature, and inclusions of other sulfide minerals. Two samples of py1 grains were mapped by the LA-ICP–MS imagining technique. The LA-ICP–MS trace element map in Fig. 10 is of a well-rounded porous py1 that is surrounded by cluster of disseminated py2. The imaging shows that the inner core of the pyrite is generally depleted in Au, Ag, Sb, Co, Ni, Bi, and Tl compared to the outer core. The elevated and spiky nature of the Au, Ag and Te in the py1 core suggests the presence of inclusions of Au–Ag-bearing tellurides, although an alternative explanation is that all three elements are dissolved in the pyrite structure via an undetermined three-way substitution mechanism (e.g., Large et al., 2013). However, the Pb map indicates inclusions of galena in the outer core that contain elevated Bi and Mo. The outer edge of py1 is marked by an irregular line of Au–Ag-rich chalcopyrite inclusions along the boundary.

The second pyrite sample selected from disseminated py1 within pyrite ± chalcopyrite–cemented breccias. LA-ICP–MS mapping (Fig. 11) highlights a zoning pattern and shows that each zone has a different trace element distribution. The anhedral core of the pyrite is enriched in Ag, Sb, Pb, Bi, Cu, and Zn. The Pb, Cu and Zn maps highlight the inclusions of Ag–Bi-rich galena, chalcopyrite and sphalerite in the core. However, the Sb map indicates that at least some of the Ag is hosted by antimony-rich end member sulfosalt (e.g., Kouhestani et al., 2012) inclusions. The As, Co, and Ni maps suggest that the core is actually a composite of two compositionally different pyrite types; an anhedral As-bearing, Co–Ni-poor type in the center core (Fig. 11c, f, g) which contains the galena, chalcopyrite, sphalerite and sulfosalt inclusions, and a subhedral As–Co–Ni-rich overgrowth type. By comparison, the Ag-rich zone is inside the euhedral Ni zone. The outermost euhedral growth of pyrite is devoid of nearly all trace elements except traces of Pb, Ni and Cu on the rim. Gold is only present in the inclusion-rich core of the pyrite composite, asso-
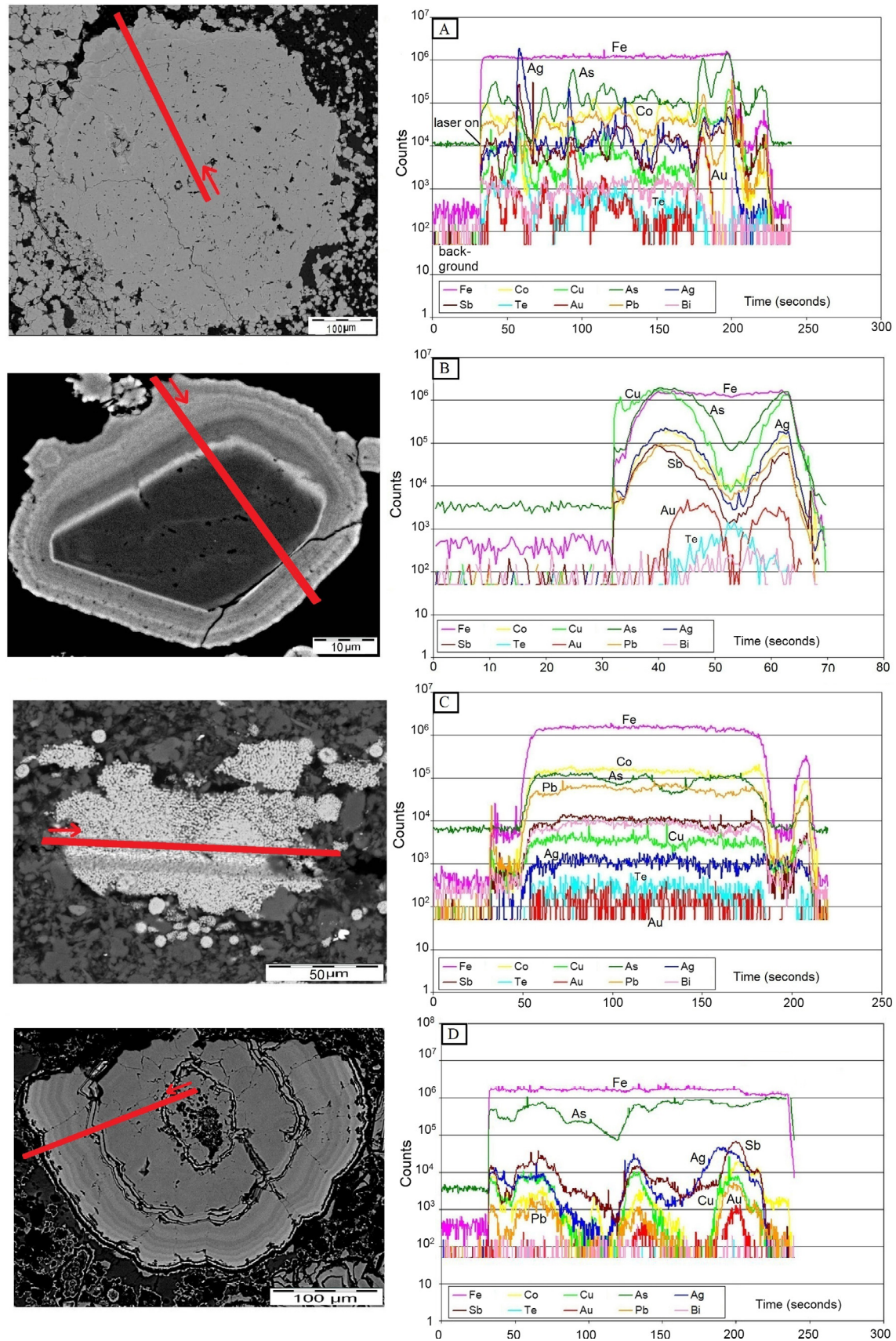
Fig. 5. LA-ICP–MS output for laser traverse across selected pyrite types at Chah Zard. Path of the laser analyses are shown on the BSE images. A. Well-rounded py1 grain; note the spiky profiles for Au, Ag, As, Sb, and Te indicating the presence of Ag-sulfosalts, electrum and Au-Ag-Te-bearing mineral microinclusions within this pyrite. B. The oscillatory-rimmed py2 with particularly high counts of Au and Ag in rims. C. Py2 framboids; note the low Au and Te values, but relatively high concentration of Ag and other trace elements. The Au, Ag, Cu, Bi, Sb, As, Pb and Co profiles fallow that of Fe suggesting that these elements are locked within the pyrite structure. D. Colloform py3; note appreciable amounts of As, but virtually no Te was detected. The profiles for Ag, Sb, Cu and Pb are parallel. Invisible gold is present as a combination of nano- to submicron-size inclusions.
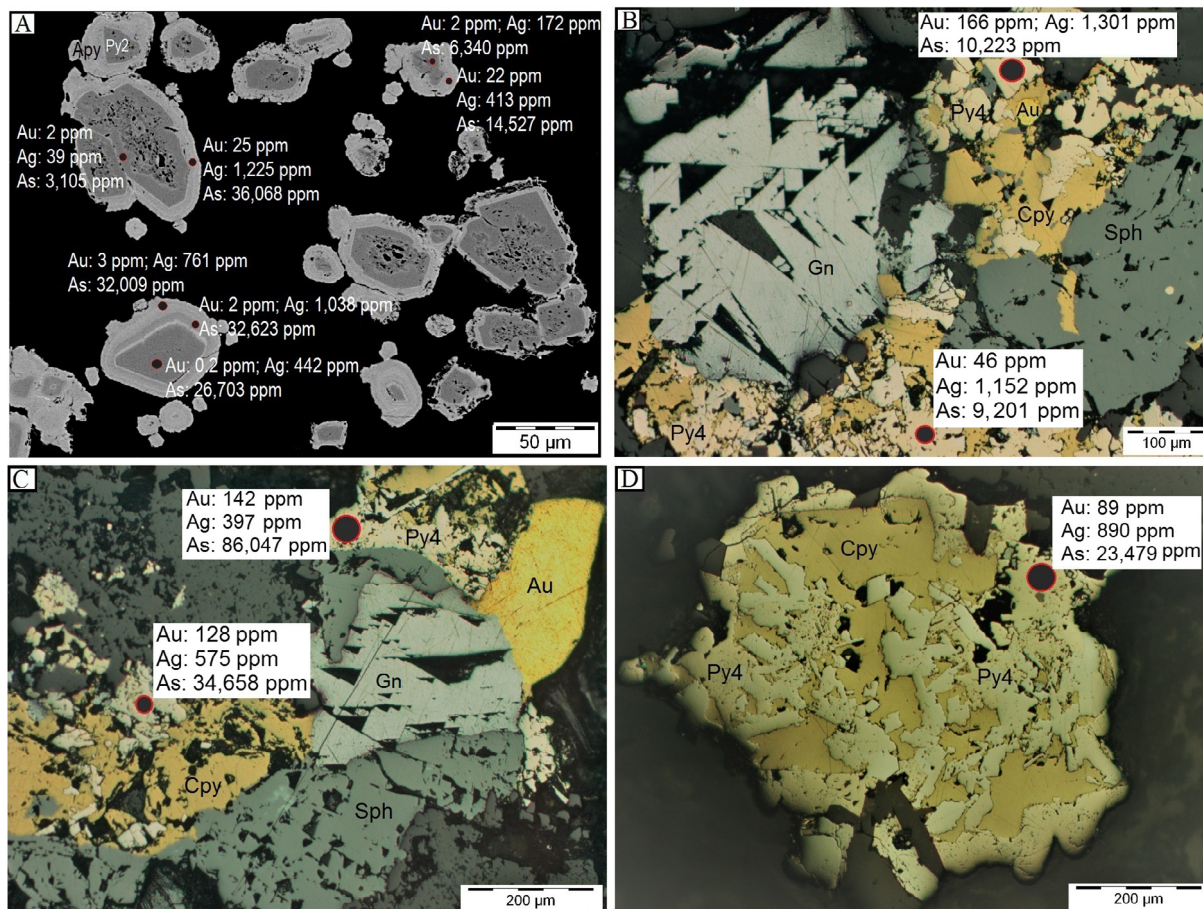
Fig. 6. Some examples of LA-ICP–MS spot analyses of gold and silver (in ppm) on different pyrite types at Chah Zard. Position of the laser spot analyses is shown in red. A. BSE image of simple-zoned and oscillatory-rimmed py2 surrounded by arsenian pyrite. B-D. Anhedral py4 intergrown with galena and sphalerite (B), gold (B, C) and chalcopyrite (C, D). The py4 has higher Au and Ag ppm values than the py2. Abbreviations as in Fig. 3.
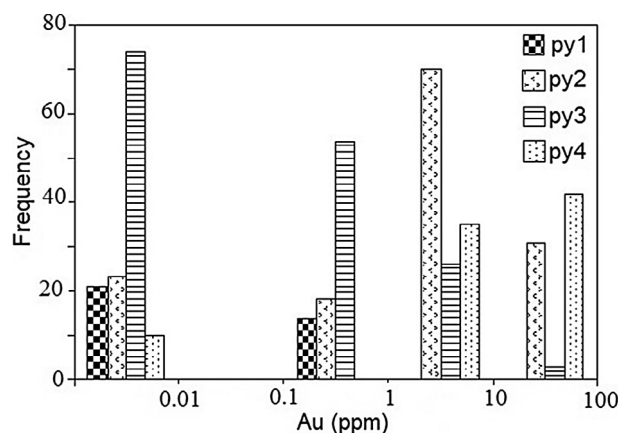
Fig. 7. Histogram (in logarithmic intervals of gold concentration) of LA-ICP–MS gold analyses for all pyrite types from the Chah Zard deposit (data summarized in Table 3). Note the highest gold content of py2 and py4, and the lowest values of py1.

ciated with elevated As and chalcopyrite, galena, sphalerite, and sulfosalt submicron inclusions. In contrast there is no detectable gold in the outer euhedral rim.

Figs. 12 and 13 are LA-ICP–MS images of gold-bearing simple-zoned and oscillatory-rimmed py2 grains, respectively, related to the main-stage (stage 2) mineralization at Chah Zard. The LA-ICP–MS map of simple-zoned py2 (Fig. 12) highlights progressive

zoning from core to rims of the pyrite and shows that each zone has a different trace element chemistry. Ag, Sb, Tl and Pb are concentrated in the pyrite core, followed by elevated Au-As-Cu in the surrounding euhedral zone, and finally a trace element depleted, high As in the outermost subhedral rim. Fig. 12g, h indicates that very thin rim on the euhedral pyrite has high Co, Ni and Ag concentrations. Tungsten and Tl are also usually elevated in the outermost pyrite rim, but other elements (particularly Au and Cu) are generally well below the levels found in the euhedral pyrite zone. The multi-element image in Fig. 13 shows that the oscillatory-rimmed py2 has a complex zonation from a trace element depleted porous core, through a subhedral inner rim enriched in Au, As, Ag, Pb, and Tl, to an As-Ag-Sb-Co-Cu-Tl-rich outermost rim. The map exhibits cyclic Ag-Sb-Co-Pb-Cu-rich and poor zones, with a general increase in As to the outermost anhedral pyrite rim. Bi and Te are present in the inner rim, whereas Mo and Cd are elevated in the outermost anhedral rim.

The LA-ICP–MS trace element map from the colloform py3 is shown in Fig. 14. The map exhibits cyclic Ag-Sb-Hg-Co-Ni-Cu-rich and poor zones, with a general increase in As to the outermost pyrite rim. The core of this pyrite is enriched in Co, Ni, and Cu, with microinclusions of electrum, Ag-sulfosalts, and chalcopyrite. The early pyrite rims are enriched in As, Ag, Sb, Co, Ni and Cu, but depleted in Zn and lacking in gold. In contrast the outermost 40-μm-thick As-rim is enriched in Au, Ag, Sb, Hg, Co, Ni, Mo, and Cu. The transition zone between the early and outermost rims shows enrichment in Tl, but depleted in Ag, Sb, Hg, Co, Ni, Cu and devoid of Au and Mo.
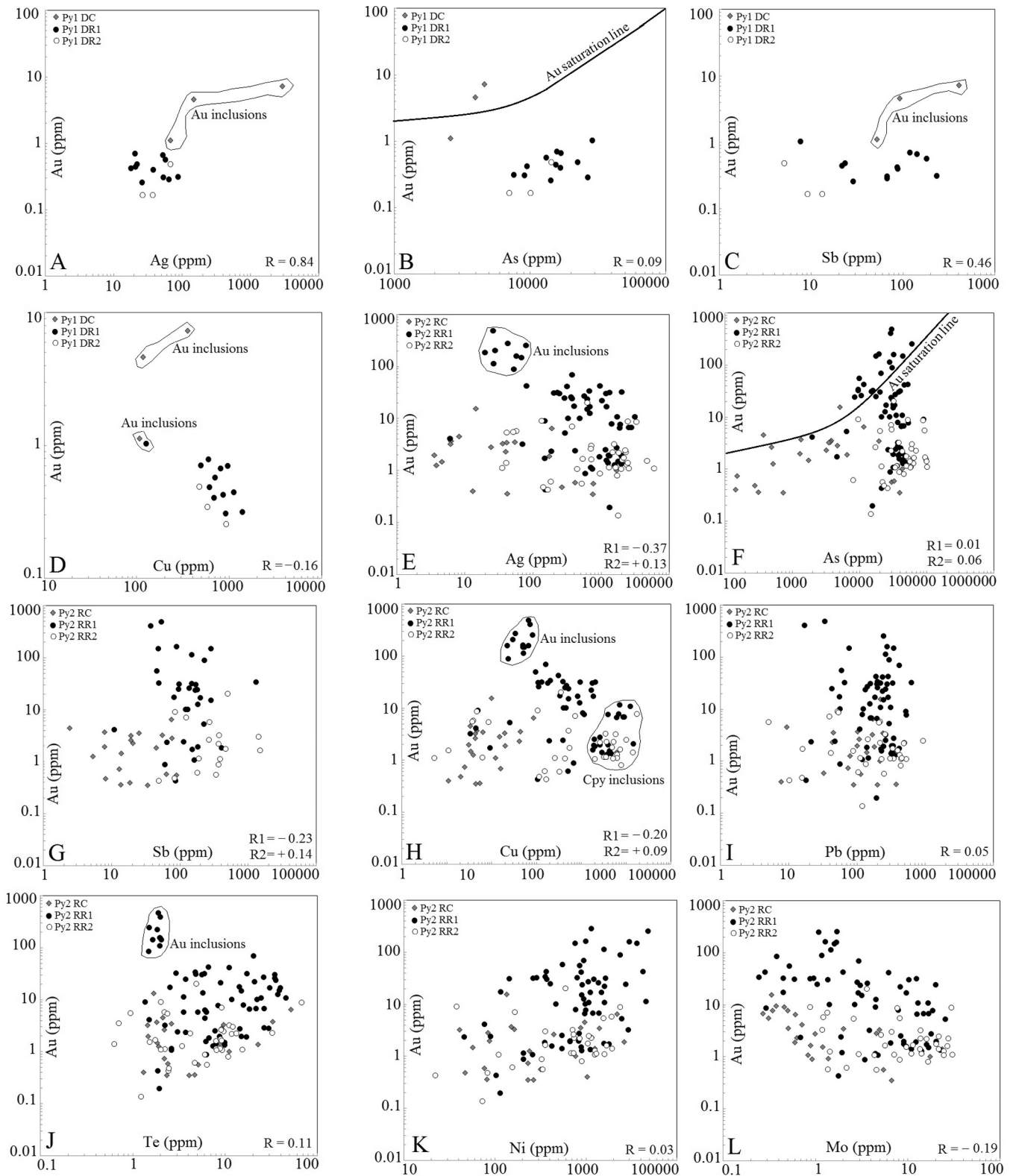
Fig. 8. Correlation between Au and other trace elements in LA-ICP–MS analyses of disseminated py1 (A-D) and oscillatory-rimmed py2 (E-L) grains. Disseminated py1 shows weak positive correlation between Au-Ag (A), Au-As (B), and Au-Sb (C), and negative correlations between Au-Cu (D). The cores of disseminated pyrite show some outlier analyses due to submicroscopic inclusions of native gold. Oscillatory-rimmed py2 shows enrichment of Au in the inner rims compared with the cores and outer rims. Note the weak positive correlation between Te and Au in oscillatory-rimmed py2 which indicates the presence of submicroscopic inclusions of Au tellurides. 0.001 was chosen for below detection values. The gold saturation line is from Reich et al. (2005). DC: disseminate-core, DR1: disseminate-inner rim, DR2: disseminate-outer rim, RC: oscillatory-rimmed-core, RR1: oscillatory-rimmed-inner rims, RR2: oscillatory-rimmed-outer rims, R: correlation coefficient, R1: correlation coefficient for inner rims, R2: correlation coefficient for outer rims.
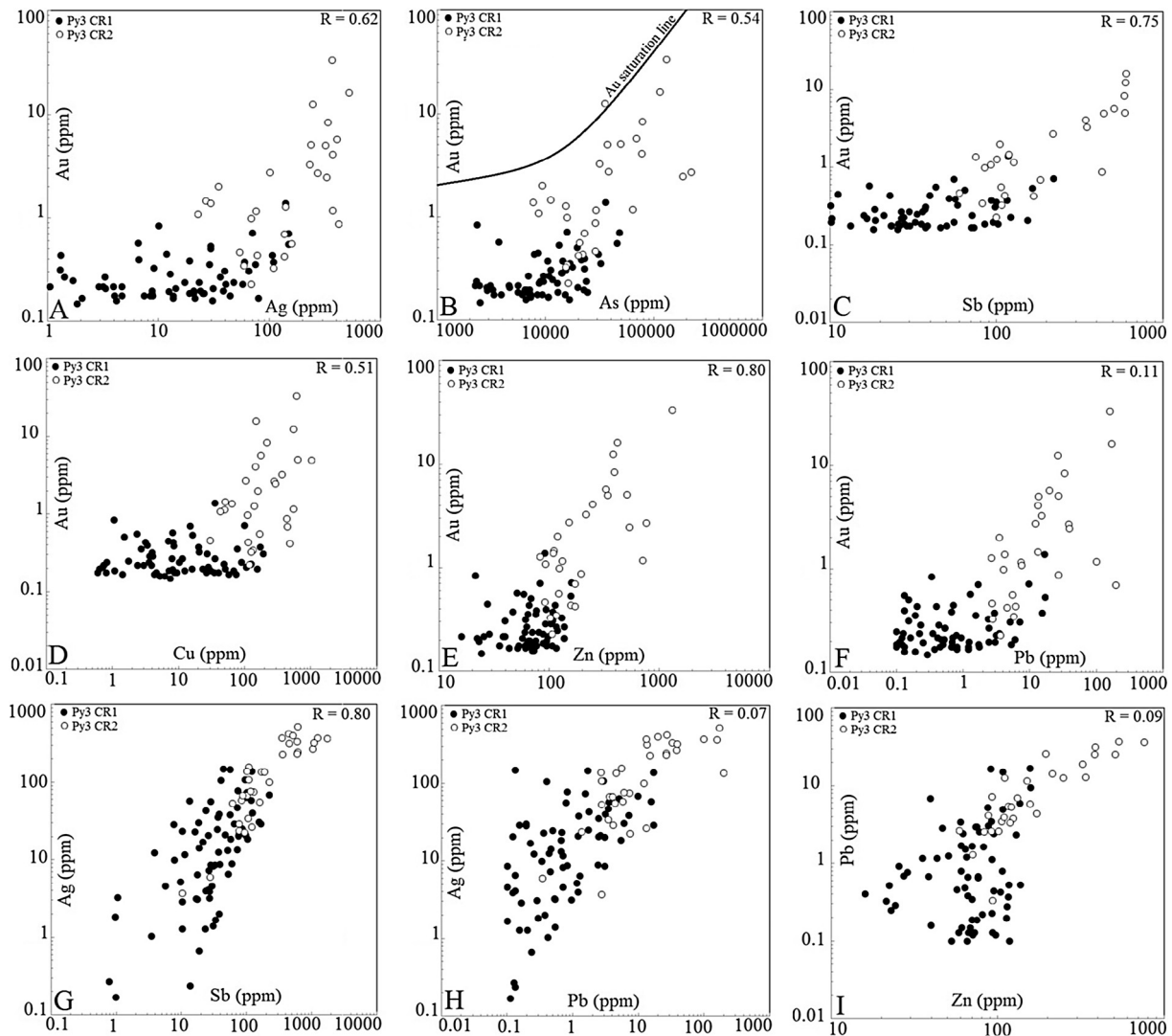
Fig. 9. Some inter-element correlations for py3 from colloform sulfide veins. Note the general depletion trends from outer rims to inner rims for Au, Ag, and most other trace elements. 0.001 was chosen for below detection values. The gold saturation line is from Reich et al. (2005). *CR1: colloform-inner rim, CR2: colloform-outer rim, R: correlation coefficient.*

8. Discussion

8.1. Textural control on gold distribution in pyrite

In the Chah Zard deposit, pyrite is the main host mineral for gold. Gold occurs within pyrite both as invisible gold in solid solution with As and micro to nanograins (native gold, electrum and Au-Ag tellurides). Based on LA-ICP–MS data, the textural evolution of pyrite at Chah Zard, from py1 to py4, is paralleled by systematic changes in the gold and trace element concentrations of the pyrite. The Au concentration in py2 and py4 is higher than that in py1 and py3 (Fig. 7). For pyrite from the same mineralization stage, different samples show similar but not identical trace element distribution and zonation.

Py1 has the lowest gold concentrations which are generally below the detection limit. This suggests that gold mineralization was extremely weak in the early stage of metallogenesis. However, the porous and fractured cores of py1 typically contain higher levels of gold (up to 6 ppm Au) and other trace elements. Most of this gold probably occurs as submicroscopic inclusions of discrete Au-bearing phases (e.g., Cook et al., 2009; Zhao et al., 2011; Large et al., 2007, 2009, 2013). Py2 usually contains significant amounts of Au and Ag, with or without relation to As and Te. The high uni-

form nature of the Au and As on LA-ICP–MS trace element maps (Figs. 12 and 13) suggest that the gold in py2 is present in solid solution in the arsenian pyrite. Spot analyses show that py2 has up to 7 wt% As and 25 ppm Au in solid solution. Colloform py3 is depleted in most trace elements. It contains low amounts of invisible gold on the rim. Whenever Au is high, As and Ag are radically enriched, with a prominent positive correlation between Au, Ag, and As (Fig. 5). However, Te is commonly very low in py3. This suggests that Au in py3, when present, occurs as invisible gold in solid solution or electrum microinclusions. In contrast, the amount of gold dissolved in the structure of py4 is significantly high based on spot analyses (Fig. 6b–d). Both As and Ag are also high, and show broad correlation with Au.

Visible gold at Chah Zard is only apparent as microscopic inclusions or stringers along the boundary of py2 and py4 (Figs. 3, 4 and 6). Gold grains contain 78.1–77.7 wt% Au and 28.5–27.2 wt% Ag, with fineness between 689 and 766 (Kouhestani, 2011). Gold is principally related to microfractures of pyrite suggesting that native gold may have resulted from mobilization of preexisting invisible gold in the structure of py2 and py4 by later-stage fluids during hydrothermal pyrite recrystallization (e.g., Bi et al., 2011; Cook et al., 2009, 2013; Large et al., 2007, 2009, 2013; Velásquez et al., 2014). The common observation of inclusions of sphalerite,
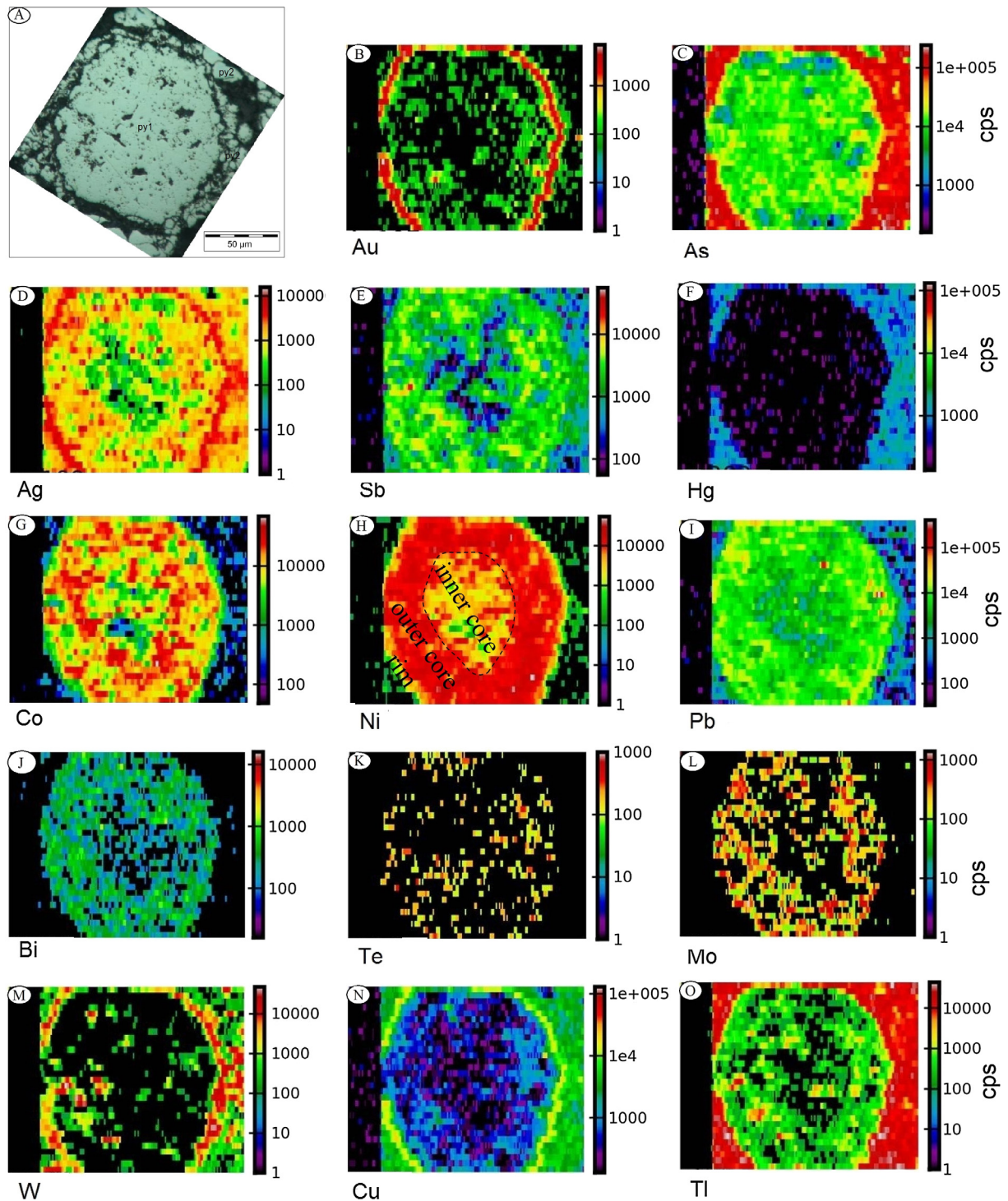
Fig. 10. LA-ICP–MS images of trace elements (counts per second, cps) in rounded py1 from Chah Zard deposit. Cluster of disseminated py2 surround the py1. The outer core of py1 is enriched in Co, Ni, Pb, Bi, Te, and Mo compared with the surrounding py2 rim. Py2 rim enriched in As, Cu, Ag, Au and Tl. The py1 has an outer rim enriched in Au, Ag and Cu.

galena and chalcopyrite in py2 and py4 at Chah Zard may be also related to this process of pyrite cleaning. In the same way that gold is released from the structure of py2 and py4 during hydrothermal recrystallization to form native gold inclusions, Cu, Pb and Zn may also be liberated from the structure of py2 and py4 to form chalcopyrite, galena and sphalerite inclusions. A similar process may account for the concentration of Au-Ag telluride and Ag–sulfosalt inclusions in py2 and the cores of py1.

8.2. Gold-arsenic relationships in pyrite

A correlation between gold and arsenic dissolved in pyrite has been recognized for some time in a range of gold deposits (e.g., Cook and Chryssoulis, 1990; Savage et al., 2000; Cline, 2001; Reich et al., 2005; Large et al., 2007, 2009, 2013). The Au-As relationships for the major pyrite types at Chah Zard are shown in Figs. 8 and 9. These show that most of the Chah Zard pyrites plot
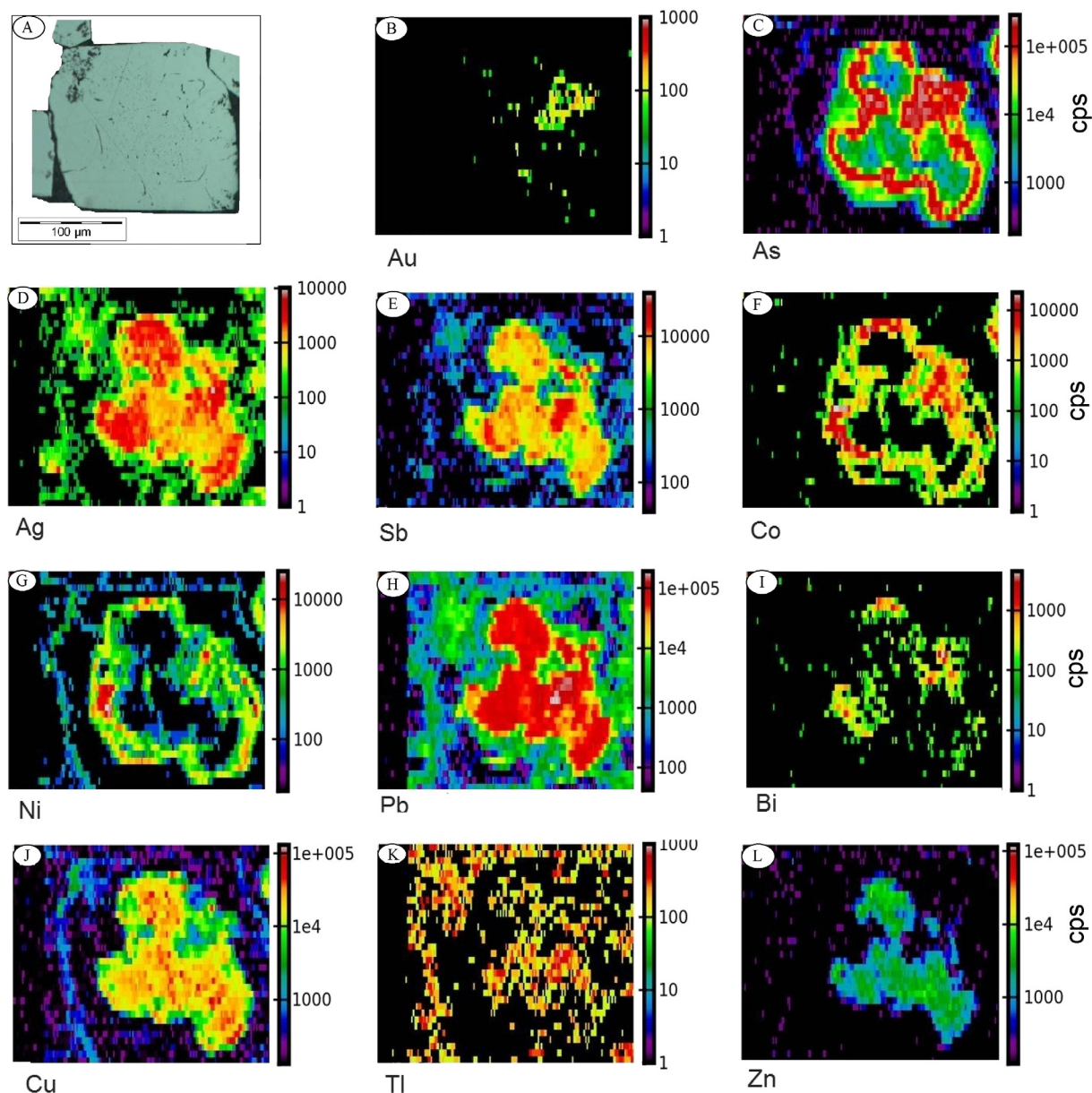
Fig. 11. LA-ICP–MS images of trace elements (cps) of disseminated py1 from Chah Zard deposit. The LA-ICP–MS maps show pyrite zonation with various elements from the core to rim. The anhedral core is enriched in Ag, Sb, Pb, Bi, Cu, and Zn. In contrast, the outer euhedral rim is depleted in most trace elements and just carries invisible Ag associated with galena inclusions. Gold is only present in the inclusion-rich core of the pyrite composite.

below the gold saturation line of Reich et al. (2005), indicating that the gold is most likely held in solid solution, as determined by the LA-ICP–MS analyses (Fig. 5). In comparison, two of the py1 cores and a significant number of the py2 rims plot above the saturation line (Fig. 8b, f), confirming the laser mapping observations that microinclusions of gold are present in py1 cores and py2 rims.

8.3. Relationship of pyrite types and zonation to evolution of the Chah Zard deposit

Based on textural and chemical differences, pyrite is a key mineral that allows Au and other metals to be traced throughout the history of formation of Au deposits (e.g., Large et al., 2009). The LA-ICP–MS spot data and maps suggest a multistage process of ore genesis at Chah Zard and indicate at least three pulses of gold enrichment during the evolution of the hydrothermal system. The early stage is accompanied by Ag, Cu, Pb, Zn, and Sb enrichment in

py1. These trace elements either occurred dissolved in the py1 structure or as nanoparticles dispersed in the py1. This stage contains only minor Au and As (Table 3), indicating that the initial fluids generated in the hydrothermal system carried little gold. However, these fluids were initially enriched in Ni and Co with minor Bi and Te. The early overgrowths of py2 contain strong Au and As enrichment, along with Cu, Cd, Tl ± Ag, Sb, Co, and Pb (Fig. 13). This Au-As event indicates a climax in gold-arsenic transport and deposition during hydrothermal fluid flow (e.g., Cook et al., 2009; Large et al., 2009, 2013). The later rims of py2 are accompanied by strong enrichments in As, Ag, Sb, Co, Pb, Cu, Ni, Mo, and Tl, along with minor Au (Fig. 13). The later hydrothermal events were accompanied by Au, As, Ag, Sb, and Cu enrichment in the very thin outermost py3 rim (Fig. 14) and py4 grains (Table 3). The thin nature of the py2 and py3 rims (2–40 μm) indicates that the hydrothermal fluid pulse was short-lived (e.g., Large et al., 2009).
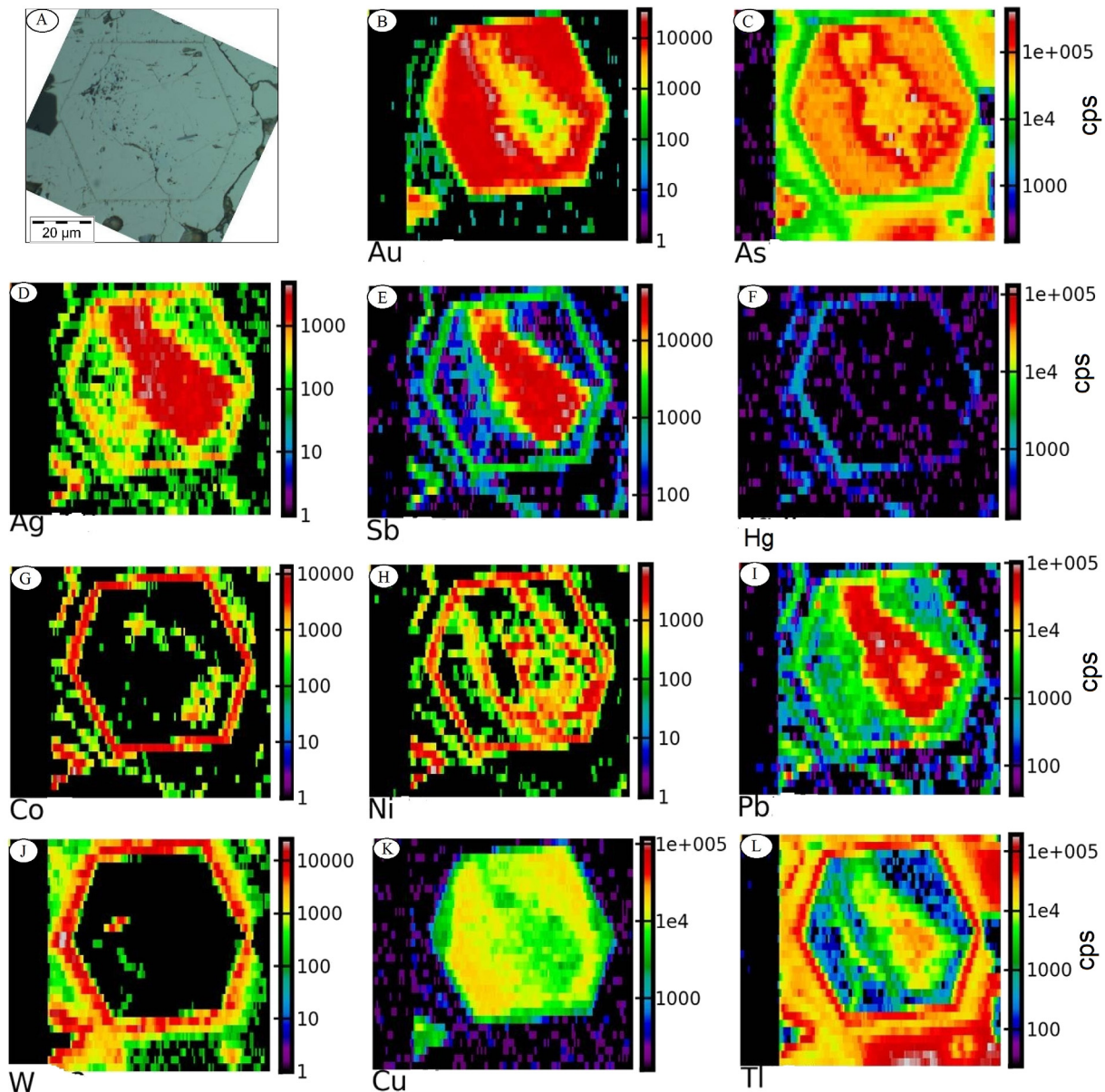
Fig. 12. LA-ICP–MS images of trace elements (cps) in simple-zoned py2 from Chah Zard deposit. The LA-ICP–MS maps indicate progressive zonation from core to rims of this pyrite. The anhedral pyrite core contains elevated Ag, Sb, and Pb. The euhedral overgrowth pyrite shows elevated Au, As, and Cu. Narrow ring around the euhedral pyrite is enriched in Co, Ni and W (g, h, j). The outermost subhedral rim is enriched in As and W, but depleted in most trace elements, compared with the euhedral pyrite generally.

8.4. Microchemical vectors to gold ore

The trace element compositions of pyrite at Chah Zard measured by LA-ICP–MS highlight systematic chemical distinction between different pyrite types. Copper and Ag display a systematic variation between the different pyrite types (Fig. 15a, b). Although the data within each pyrite type range over two to five orders of magnitude, the results suggest that there is over one to two orders of magnitude variation between the different pyrite types. There is a significant decrease in concentration of both elements in py1 and py3 compared with those values observed in the py2 and py4. Lead shows an overall decrease in concentration from py4 through the py1 and py2 and into the py3 (Fig. 15c). The use of Cu/Pb and Pb/Ag ratios further discriminates different pyrite types (Fig. 15d). There is a noteworthy increase in Cu/Pb ratio from py1 through the py4 and into the py3 and py2. These systematic chemical variations in the trace

element composition of different pyrite types need to be observed for the potential application of the technique to be used as a vector to epithermal gold mineralization in the Chah Zard. Additional research, however, is required to ascertain this chemical zonation in pyrites from different alteration zones to establish its lateral and vertical extension, and indeed whether a similar pattern is observed for parts of the system that are hosted by the same alteration zones.

8.5. Implications for ore genesis

The textural and trace element composition of pyrite can be used as a potential application of the technique to be used as a vector to ore (e.g., Baker et al., 2006). These data provide evidence for the overlapping/overprinting of events and their different impact on Au redistribution (e.g., Cook et al., 2009). The LA-ICP–MS data for gold distribution at Chah Zard indicate that only minor Au
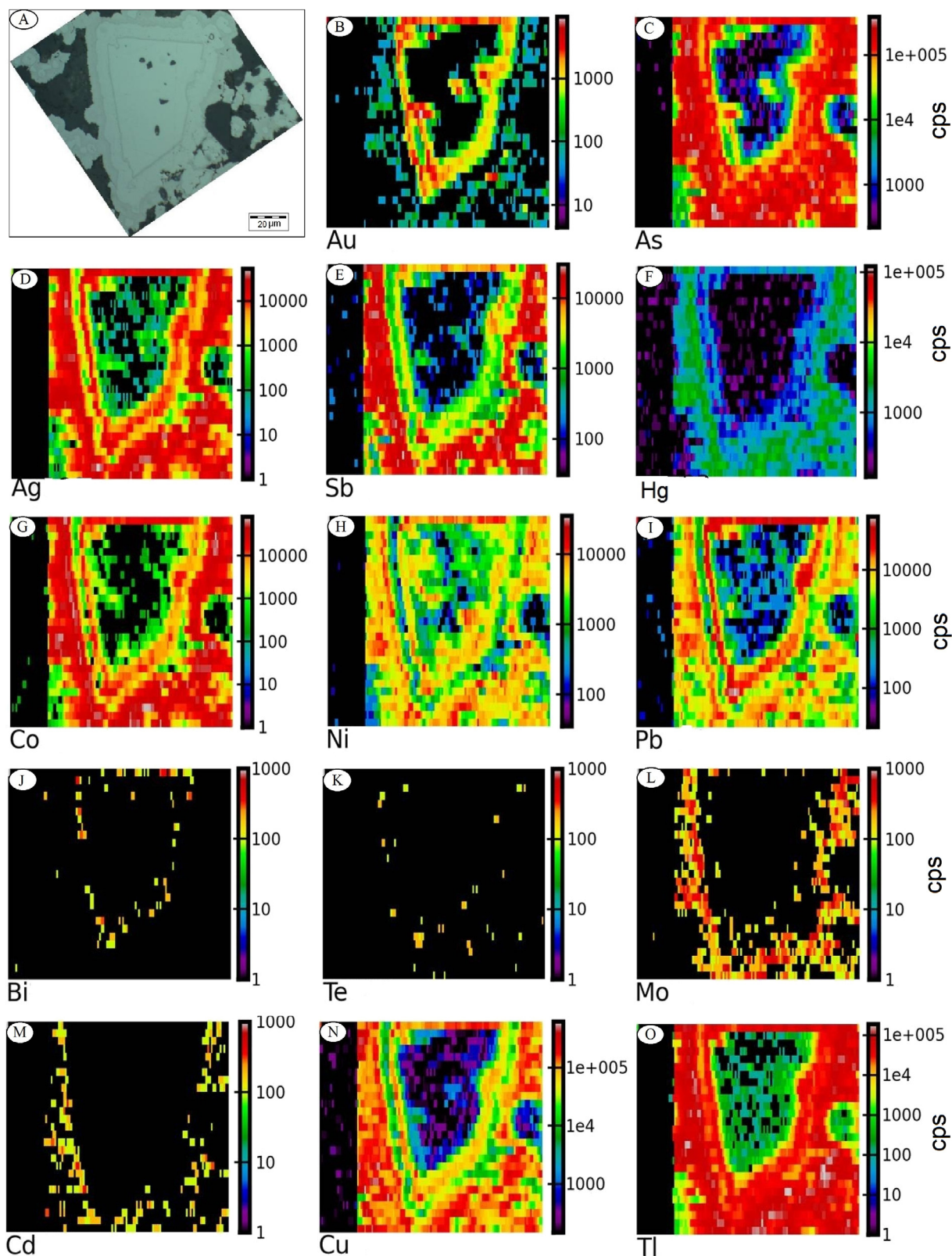
Fig. 13. LA-ICP–MS images of trace elements (cps) of oscillatory-rimmed py2 from Chah Zard deposit. This pyrite contains a porous core surrounded by two ∼10-μm-thick pyrite rims. The core contains inclusion of chalcopyrite and galena. Au image shows red-yellow spot in core due to inclusions of native gold. The images show that the subhedral inner rim contains elevated Au, As, Ag, and Pb. The anhedral outermost pyrite rim is enriched in As, Ag, Sb, Co, and Cu.

was originally trapped in py1 from the initial ore fluids. It is, how-ever, certain that the initial fluids were enriched in other trace ele-ments such as Ag, Cu, Pb, Zn, and Sb. The high Co–Ni signatures of

py1 support an origin from a magmatically-derived hydrothermal system and also point at a local influence of other metal sources. One might speculate that these higher Co and Ni contents at Chah
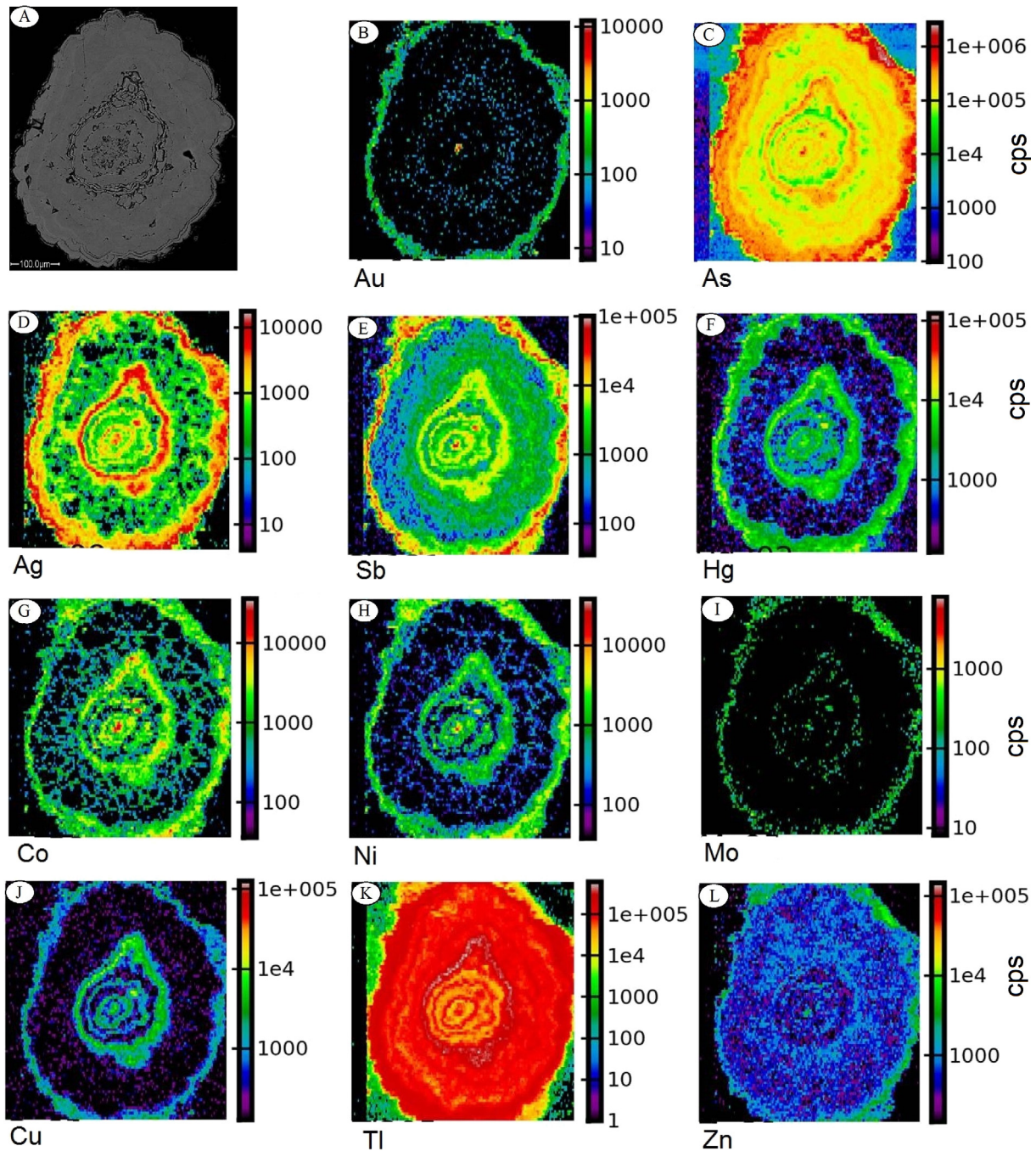
Fig. 14. LA-ICP–MS images of trace elements (cps) in colloform py3 from Chah Zard deposit. The core of this pyrite is enriched in Co, Ni, and Cu, with spiky inclusions of Au, and Ag related to electrum, Ag-sulfosalts, and chalcopyrite microinclusions. The early pyrite rims show As-Ag-Sb-Co-Ni-Cu enrichment but are depleted in Zn and lacking in gold. The 40-μm-thick outermost As-rim is enriched in Au, Ag, Sb, Hg, Co, Ni, Mo, and Cu.

Zard could reflect local leaching from the mafic units of the ophi-olitic complex, which are exposed in the southwestern part of the area (Kouhestani, 2011). This is consistent with the conclusion by Kouhestani et al. (2015) who documented that Chah Zard pyrite has slightly positive δ³⁴S values (consistent with a magmatic ori-gin) and that quartz has a low oxygen isotope signature, indicating isotope exchange between magmatic and meteoritic waters.

The gold in the py1 was mobilized during overprinting hydrothermal events that involved fracturing and brecciation (Fig. 3a, b). This is indicated by the observation that the porous and brecciated domains of py1 contain higher Au concentration (up to 6 ppm). Kouhestani (2011) also states that fractured zones

of py1 mostly contain higher levels of gold and other trace ele-ments. This phenomenon is common and has been also suggested by other researchers (e.g., Cook et al., 2009; Zhao et al., 2011; Large et al., 2009, 2013). We speculate that higher Au concentrations in the porous or fractured py1 are caused by collateral ablation of minute inclusions located in the microfissures of pyrite. Most of this gold is probably not incorporated into the pyrite structure but occurs as minute, submicroscopic inclusions of discrete Au-bearing phases within pores and interstices of the porous pyrite. We cannot exclude the possibility, however, that small amounts of Au were incorporated into the pyrite structure or the interstices when other elements (such as As, Te and Sb) distorted the pyrite
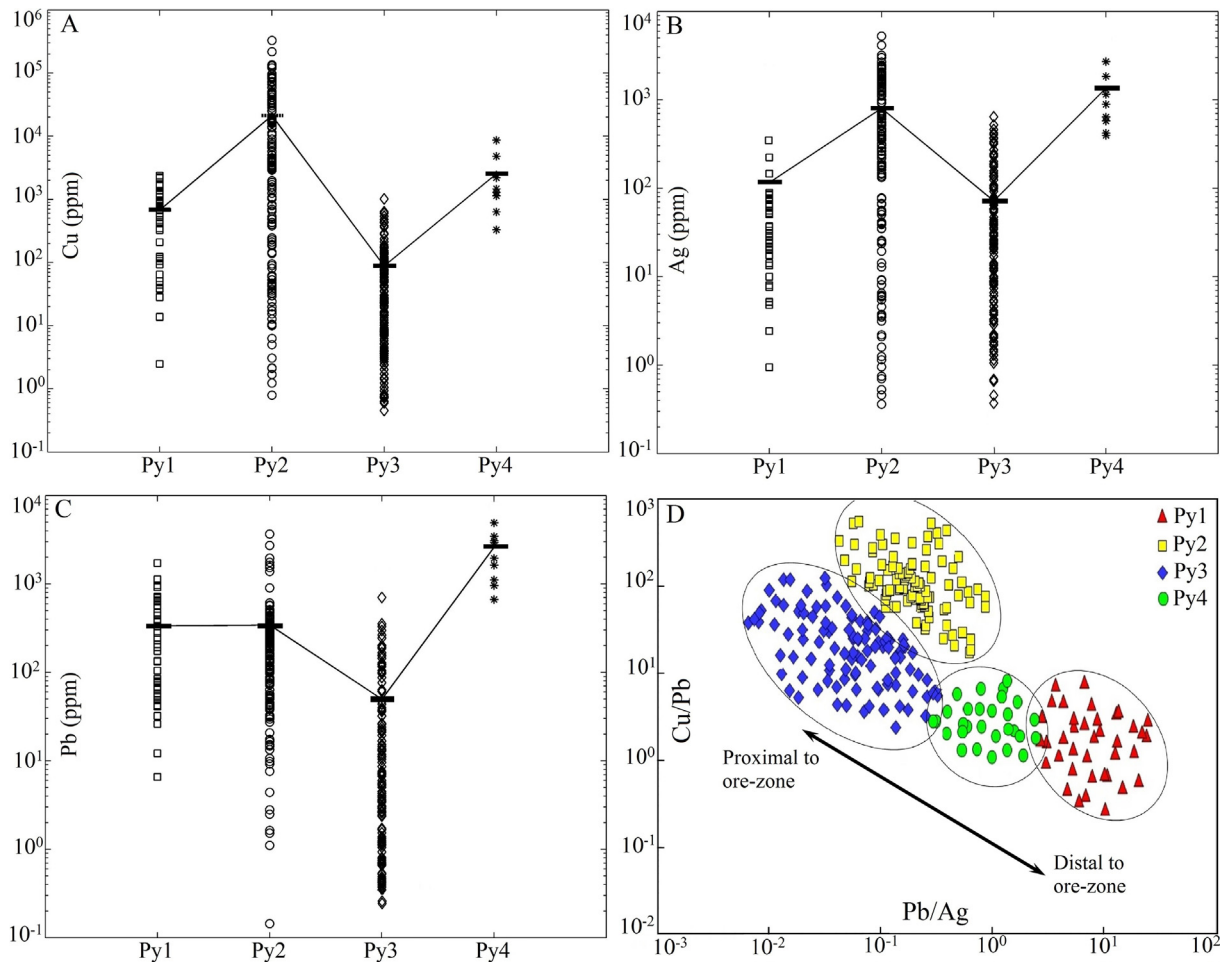
Fig. 15. A–C. Selected elements that show systematic variations in concentration between the different pyrite types including Cu (A), Ag (B) and Pb (C). Mean averages of data are linked between pyrite types to illustrate the systematic trends. D. Scatter plot of Cu/Pb and Pb/Ag ratios illustrate distinct differences between the different pyrite types.

structure to allow Au to enter (e.g., Cook et al., 2009; Zhao et al., 2011). The LA-ICP–MS results, however, supposes that most, if not all, Au and associated metals at Chah Zard were transported and deposited during sequential overprinting hydrothermal fluid flow. This is supported by hydrothermal overgrowth pyrite rims and grains, here classified as py2 and py4, that usually contain strong Au, As, and Ag enrichment. These results are consistent with and complement those of Cook et al. (2009) and Large et al. (2009, 2013), who also considered that textural and geochemical evidence in pyrite demonstrate cycles of hydrothermal infiltration, and remobilization during evolution of gold ores. Kouhestani (2011) also states that the presence of py2 and py4 in the vein and breccia–cemented ores is an excellent indication of elevated gold grade.

The ore-forming model for gold distribution presented above suggest that the Chah Zard hydrothermal system must have been protracted and must have involved repeated pulses of mineralizing fluids at different stages during its evolution. This model is in accordance with the previous geological, fluid inclusion and stable isotopic evidence (Kouhestani et al., 2012, 2015). Kouhestani et al. (2015) indicate that the Chah Zard gold deposit has been a result of two consecutive episodes of mineralization, with gold mainly formed in the late mineralization stages. The more saline initial fluids associated with rhyolitic magmas resulted in low gold concentrations in py1 within the areas of magmatic-hydrothermal breccias (Kouhestani et al., 2012, stage 1). Clasts of this stage were found as brecciated and rounded py1 grains in later mineralization

stages (Kouhestani et al., 2012). The main gold-transporting liquid during ore stages (stages 2, 3 and 4) was moderately saline, and is thought to have a magmatic source (Kouhestani et al., 2015). Boiling of this fluid and its mixing with meteoric waters resulted in the highest gold concentrations in py2 and py4, and locally, py3 within breccia (i.e., polymictic, and mixed monomictic to polymictic) cements, and veins cutting breccia bodies. The zonation patterns of py2 and py3 reflect fluctuations in the hydrothermal fluid chemistry as magmatic and meteoric waters mixed in variable proportions.

9. Concluding remarks

Our textural observations and LA-ICP–MS data demonstrate the occurrence of complex textures and the presence of chemical zones in pyrite at Chah Zard, showing a protracted evolution and overlapping hydrothermal events. The results pinpoint several patterns of gold redistribution, and highlight the importance of multistage concentration of gold in the genesis of Chah Zard epithermal gold deposit.

There are systematic trace element differences between distinct pyrite types. Py1, preceding the main gold mineralization, contains highest Ni and Co concentrations, but lowest invisible gold. Nonetheless, the porous and fractured cores of py1 mostly contain higher levels of invisible gold which is likely related to minute gold inclusions in the pore space of the respective pyrite grains. Py2 and

py4 represent the main gold mineralization, and show the significant amounts of invisible gold, with a prominent positive correlation between Au, Ag, As, and Te. Py3 has small amounts of invisible gold, possibly present as nanoparticle inclusions of electrum. Visible gold is widespread along grain boundaries or in the microfractures of py2 and py4 most likely resulting from local remobilization and recrystallization of precursor invisible gold.

Our LA-ICP–MS data have provided insight into trace element chemistry of different pyrite types and suggests that three elements, Cu, Pb and Ag, show systematic variations between the pyrite types; ratios of these elements may provide a potentially powerful exploration vector to epithermal gold mineralization in the Chah Zard and elsewhere. Interestingly, whole-rock chemistry from the different mineralizing zones does not show a similar pattern (Kouhestani, 2011), suggesting that the results are unique to the pyrite rather than the bulk rock chemistry. Results of this study support previous notions that LA-ICP–MS study of gold distribution in texturally different pyrite types not only provides valuable information on the distribution pattern of gold, but also in understanding the processes of gold deposition and evolution.

Acknowledgements

References

Agangi, A., Hofmann, A., Wohlgemuth-Ueberwasser, C.C., 2013. Pyrite zoning as a record of mineralization in the Ventersdorp Contact Reef, Witwatersrand Basin, South Africa. Econ. Geol. 108, 1243–1272.

Agard, P., Omrani, J., Jolivet, L., Mouthereau, F., 2005. Convergence history across Zagros (Iran): constraints from collisional and earlier deformation. Int. J. Earth Sci. 94, 401–419.

Agard, P., Omrani, J., Jolivet, L., Whitechurch, H., Vrielynck, B., Spakman, W., Monié, P., Meyer, B., Wortel, R., 2011. Zagros orogeny: a subduction-dominated process. Geol. Mag. 148, 692–725.

Alavi, M., 1994. Tectonics of the Zagros orogenic belt of Iran: new data and interpretations. Tectonophysics 229, 211–238.

Baker, T., Mustard, R., Brown, V., Pearson, N., Stanley, C.R., Radford, N.W., Butler, I., 2006. Textural and chemical zonation of pyrite at Pajingo: a potential vector to epithermal gold veins. Geochem. Explor. Environ. Anal. 6, 283–293.

Berberian, F., Berberian, M., 1981. Tectono-plutonic episodes in Iran. In: Gupta, H.K., Delany, F.M. (Eds.), Zagros-Hindu Kush–Himalaya Geodynamic Evolution. American Geophysical Union and Geological Society of America, Washington, pp. 5–32.

Berberian, M., King, G.C.P., 1981. Towards a paleogeography and tectonic evolution of Iran. Can. J. Earth Sci. 18, 210–265.

Berberian, F., Muir, I.D., Pankhurst, R.J., Berberian, M., 1982. Late Cretaceous and Early Miocene Andean-type plutonic activity in northern Makran and Central Iran. J. Geol. Soc. London 139, 605–614.

Bi, S.J., Li, J.W., Zhou, M.F., Li, Z.K., 2011. Gold distribution in As-deficient pyrite and telluride mineralogy of the Yangzhaiyu gold deposit, Xiaoqinling district, southern North China Craton. Miner. Deposita 46, 925–941.

Bina, M.M., Bucur, I., Prevot, M., Meyerfeld, Y., Daly, L., Cantagrel, J.M., Mergoil, J., 1986. Palaeomagnetism petrology and geochronology of Tertiary magmatic and sedimentary units from Iran. Tectonophysics 121, 303–329.

Cline, J.S., 2001. Timing of gold and arsenic sulfide mineral deposition at the Getchell Carlin-type gold deposit, north central Nevada. Econ. Geol. 96, 75–89.

Cook, N.J., Chryssoulis, S.L., 1990. Concentrations of invisible gold in the common sulfides. Can. Mineral. 28, 1–16.

Cook, N.J., Ciobanu, C.L., Mao, J.W., 2009. Textural control on gold distribution in As-free pyrite from the Dongping, Huangtuliang and Hougou gold deposits, North China Craton (Hebei Province, China). Chem. Geol. 264, 101–121.

Cook, N.J., Ciobanu, C.L., Meria, D., Silcock, D., Wade, B., 2013. Arsenopyrite-pyrite association in an orogenic gold ore: tracing mineralization history from textures and trace elements. Econ. Geol. 108, 1273–1283.

Danyushevsky, L.V., Robinson, P., McGoldrick, P., Large, R.R., Gilbert, S., 2003. LA-ICPMS of sulphides: evaluation of an XRF glass disc standard for analysis of different sulphide matrixes [abs.]: 2003 Goldschmidt Conference, Japan. Geochim. Cosmochim. Acta 67, 23.

Dargahi, S., Arvin, M., Yuanming, P., Babaei, A., 2010. Petrogenesis of post-collisional A-type granitoids from the Urumieh-Dokhtar magmatic assemblage Southwestern Kerman Iran: constraints on the Arabian-Eurasian continental collision. Lithos 115, 190–204.

Ghaderi, M., Kouhestani, H., Chang, Z., Zaw, K., 2012a. Fluid inclusion and stable isotope study of the Chah Zard breccia-hosted epithermal gold-silver deposit, west-central Iran [ext. abs.]. In: International Geological Congress (IGC), 34th, Brisbane, Australia, 2012, Extended Abstracts, p. 2036.

Ghaderi, M., Kouhestani, H., Zaw, K., Mernagh, T., 2012b. Fluid inclusion microthermometry and Raman spectroscopic analysis of the Chah Zard epithermal gold-silver deposit, west central Iran [ext. abs.]. In: Asian Current Research on Fluid Inclusions, ACROFI IV, Brisbane, Australia, 2012, Extended Abstracts, p. 29.

Koglin, N., Frimmel, H.E., Minter, W.E.L., Brätz, H., 2010. Trace-element characteristics of different pyrite types in Mesoarchaean to Palaeoproterozoic placer deposits. Miner. Deposita 45, 259–280.

Kouhestani, H., 2011. Geology, Alteration, Isotope Geochemistry and Origin of Chah Zard Ag-Au Deposit Southwest of Yazd (Unpublished Ph.D. thesis). Tarbiat Modares University, Tehran, Iran, pp. 285.

Kouhestani, H., Ghaderi, M., Zaw, K., Meffre, S., Emami, M.H., 2012. Geological setting and timing of the Chah Zard breccia-hosted epithermal gold-silver deposit in the Tethyan belt of Iran. Miner. Deposita 47, 425–440.

Kouhestani, H., Ghaderi, M., Chang, Z., Zaw, K., 2015. Constraints on the ore fluids in the Chah Zard breccia-hosted epithermal Au–Ag deposit, Iran. Fluid inclusions and stable isotope studies. Ore Geol. Rev. 65, 512–521.

Large, R.R., Maslennikov, V., Robert, F., Danyushevsky, L.V., Chang, Z., 2007. Multistage sedimentary and metamorphic origin of pyrite and gold in the giant Sukhoi Log deposit, Lena gold province, Russia. Econ. Geol. 102, 1232–1267.

Large, R.R., Danyushevsky, L., Hollit, C., Maslennikov, V., Meffre, S., Gilbert, S., Bull, S., Scott, R., Emsbo, P., Thomas, H., Singh, B., Foster, J., 2009. Gold and trace element zonation in pyrite using a laser imaging technique: Implications for the timing of gold in orogenic and Carlin-style sediment-hosted deposits. Econ. Geol. 104, 635–668.

Large, R.R., Meffre, S., Burnett, R., Guy, B., Bull, S., Gilbert, S., Geomann, K., Danyushevsky, L.V., 2013. Evidence for an intrabasinal source and multiple concentration processes in the formation of the Carbon Leader Reef, Witwatersrand Supergroup, South Africa. Econ. Geol. 108, 1215–1241.

Longerich, H.P., Jackson, S.E., Gunther, D., 1996. Laser ablation inductively coupled plasma mass spectrometric transient signal data acquisition and analyte concentration calculation. J. Anal. At. Spectrom. 11, 899–904.

Omrani, J., Agard, P., Whitechurch, H., Benoit, M., Prouteau, G., Jolivet, L., 2008. Arc-magmatism and subduction history beneath the Zagros Mountains, Iran: a new report of adakites and geodynamic consequences. Lithos 106, 380–398.

Przybyłowicz, W.J., Prozesky, V.M., Meyer, F.M., 1995. True elemental imaging of pyrites from Witwatersrand reefs. Nucl. Instrum. Methods Phys. Res. Sect. B 104, 450–455.

Reich, M., Kesler, S.E., Utsunomiya, S., Palenik, C.S., Chryssoulis, S.L., Ewing, R., 2005. Solubility of gold in arsenian pyrite. Geochim. Cosmochim. Acta 69, 2781–2796.

Reimold, W.U., Przybyłowicz, W.J., Gibson, R.L., 2004. Quantitative major and trace elemental mapping by PIXE of concretionary pyrite from the Witwatersrand Basin, South Africa. X-Ray Spectrom. 33, 189–203.

Richards, J.P., Boyce, A.J., Pringle, M.S., 2001. Geologic evolution of the Escondida area, northern Chile: a model and temporal localization of porphyry Cu mineralization. Econ. Geol. 96, 271–305.

Richards, J.P., Wilkinson, D., Ullrich, T., 2006. Geology of the Sari Gunay epithermal gold deposit, northwest Iran. Econ. Geol. 101, 1455–1496.

Savage, K.S., Tingle, T.N., O'Day, P.A., Waychunas, G.A., Bird, D.K., 2000. Arsenic speciation in pyrite and secondary weathering phases, Mother lode gold district, Tuolumne County California. Appl. Geochem. 15, 1219–1244.

Sengör, A.M.C., 1990. A new model for the Late Paleozoic-Mesozoic tectonic evolution of Iran and implication for Oman region. Geol. Soc. London Spec. Publ. 49, 797–831.

Shahabpour, J., 2007. Island-arc affinity of the Central Iranian volcanic belt. J. Asian Earth Sci. 30, 652–665.

Tosdal, R.M., Richards, J.P., 2001. Magmatic and structural controls on the development of porphyry Cu ± Mo ± Au deposits. Rev. Econ. Geol. 14, 157–181.

Velásquez, G., Béziat, D., Salvi, S., Siebenaller, L., Borisova, A.Y., Pokrovski, G.S., Parseval, P.D., 2014. Formation and deformation of pyrite and implications for gold mineralization in the El Callao district, Venezuela. Econ. Geol. 109, 457–486.

Zhao, H.X., Frimmel, H.E., Jiang, S.Y., Dai, B.Z., 2011. LA-ICP-MS trace element analysis of pyrite from the Xiaoqinling gold district, China: Implications for ore genesis. Ore Geol. Rev. 43, 142–153.